AGN photoionization of gas in companion galaxies as a probe of AGN radiation in time and direction

William C. Keel,[1,2,3]⋆ Vardha N. Bennert,[4] Anna Pancoast,[5,6]† Chelsea E. Harris,[5,7] Anna Nierenberg,[1,5,8]‡ S. Drew Chojnowski,[9] Alexei V. Moiseev [10,11,12] Dmitry V. Oparin,[10] Chris J. Lintott [13,14] Kevin Schawinski,[15] Graham Mitchell[16] and Claude Cornen[16]

[1]*Department of Physics and Astronomy, University of Alabama, Box 870324, Tuscaloosa, AL 35487, USA*
[2]*Kitt Peak National Observatory, operated by AURA, Inc., under contract to the US National Science Foundation*
[3]*SARA Observatory, Embry-Riddle Aeronautical University, Daytona Beach, FL 32214, USA*
[4]*Department of Physics, California Polytechnic State University, San Luis Obispo, CA 93407, USA*
[5]*Department of Physics, University of California, Santa Barbara, CA 93106 USA*
[6]*Harvard-Smithsonian Center for Astrophysics, 60 Garden St., Cambridge, MA 02138. USA*
[7]*Department of Energy Computational Science Graduate Fellow, Department of Astronomy, University of California, Berkeley, CA 94720, USA*
[8]*Center for Cosmology and AstroParticle Physics, 191 West Woodruff Avenue, The Ohio State University, Columbus, OH 43204, USA*
[9]*Department of Astronomy, New Mexico State University, Las Cruces, NM 11001, USA*
[10]*Special Astrophysical Observatory, Russian Academy of Sciences, Nizhny Arkhyz 369167, Russia*
[11]*Lomonosov Moscow State University, Sternberg Astronomical Institute, Universitetsky pr. 13, Moscow 119234, Russia*
[12]*Space Research Institute, Russian Academy of Sciences, Profsoyuznaya ul. 84/32, Moscow 117997, Russia*
[13]*Astrophysics, Oxford University, Oxford, UK*
[14]*Adler Planetarium, 1300 S. Lakeshore Drive, Chicago, IL 60605, USA*
[15]*Department of Physics, ETH Zürich, Switzerland*
[16]*Galaxy Zoo, Oxford University, Oxford, UK*

ABSTRACT

We consider active galactic nucleus (AGN) photoionization of gas in companion galaxies (cross-ionization) as a way to sample the intensity of AGN radiation in both direction and time, independent of the gas properties of the AGN host galaxies. From an initial set of 212 AGN+companion systems, identified with the help of Galaxy Zoo participants, we obtained long-slit optical spectra of 32 pairs that were *a priori* likely to show cross-ionization based on projected separation or angular extent of the companion. From emission-line ratios, 10 of these systems are candidates for cross-ionization, roughly the fraction expected if most AGNs have ionization cones with 70° opening angles. Among these, Was 49 remains the strongest nearby candidate. NGC 5278/9 and UGC 6081 are dual-AGN systems with tidal debris, complicating identification of cross-ionization. The two weak AGNs in the NGC 5278/9 system ionize gas filaments to a projected radius 14 kpc from each galaxy. In UGC 6081, an irregular high-ionization emission region encompasses both AGNs, extending more than 15 kpc from each. The observed AGN companion galaxies with and without signs of external AGN photoionization have similar distributions in estimated incident AGN flux, suggesting that geometry of escaping radiation or long-term variability controls this facet of the AGN environment. This parallels conclusions for luminous QSOs based on the proximity effect among Lyman α absorbers. In some galaxies, mismatch between spectroscopic classifications in the common BPT diagram and the intensity of weaker He II and [Ne V] emission lines highlights the limits of common classifications in low-metallicity environments.

Key words: galaxies: active – galaxies: ISM – galaxies: Seyfert.

E-mail: wkeel@bama.ua.edu, wkeel@ua.edu
† Einstein Fellow.
‡ CCAPP Fellow.

1 INTRODUCTION

Important aspects of active galactic nuclei (AGNs) can be studied through the properties of surrounding gas on scales up to kiloparsecs, providing information otherwise inaccessible due to the small size of the central regions or the time-scales involved. This is especially true for AGN with extended emission-line regions (EELRs), which span tens of kiloparsecs in radial distance and often occur over broad angular ranges about the central source (Stockton, Fu & Canalizo 2006). The frequent occurrence of (double) ionized clouds with triangular shapes ('ionization cones') was a key piece of evidence for some form of geometric unification involving Seyfert galaxies of types 1 and 2 (Antonucci 1993). Recently, the discovery of the 45-kpc cloud known as Hanny's Voorwerp (Lintott et al. 2009; Schawinski et al 2010; Keel et al. 2012b; Schawinski et al 2015; Sartori et al. 2016) highlighted what had earlier been an abstract possibility: using EELRs to trace the history of radiation from AGN across the light-travel times to distant gas clouds. In this object, the gas is so highly ionized that it must be illuminated by a luminous quasar, 2 orders of magnitude brighter than the observed galaxy nucleus; a former quasar has faded dramatically within the $\approx 10^5$-yr light-travel time between the central AGN and the cloud edge. A tailored search by Galaxy Zoo participants led to confirmation of 19 less luminous examples (Keel et al. 2012a), while later studies have identified analogous candidates for fading AGN detected via such ionization echoes at both lower and higher luminosity (Schirmer et al. 2013; Schweizer et al. 2013; Watkins et al. 2018).

The use of EELR gas to determine properties of the AGN is restricted by the distribution of the gas around the AGN host galaxy. The escape of radiation may suffer from biases due to both the relative orientations of the disc and AGN absorbing torus (whose axes are essentially uncorrelated; Schmitt et al. 2003) and to obscuration from dust in the galaxy disc; there must be distant gas in directions where the AGN radiation is not blocked by material in the host. Indeed, in Hanny's Voorwerp and its fainter Galaxy Zoo analogues, the EELRs are part of tidal debris (Keel et al. 2015). In this study, we explore a kind of EELR that is not directly related to the AGN host - gas in companion galaxies. EELRs of this kind would not suffer the same biases in illumination, and would also not have the kind of radial density structure that might be found in gas associated with the AGN host itself; the distribution of gas in the companion would still control where it could be ionized, but now in a way not correlated with the AGN's structure. These kinds of decoupling from the AGN host structure might allow more secure measurements of the angular pattern of escaping radiation, and its time history, than are possible from ionization of gas within the AGN host itself. While the details of triggering AGN by galaxy interactions remain contentious, many AGNs are certainly located in close (and often-interacting) galaxy pairs, so we can use companion galaxies as screens to view the emerging radiation from their active neighbors, which for convenience we will call cross-ionization.

The conditions needed for cross-ionization in galaxy pairs to occur were set out as early as Filippenko (1982), and have been briefly considered again in connection with growing interest in dual-AGN systems (Liu et al. 2011). In spectra with large apertures, cross-ionization could mimic a relatively low-luminosity AGN (as was noted by Liu et al. 2011), while ionized gas from a companion could generate velocity asymmetries in survey spectra of the kind studied by Comerford & Greene (2014). One of the best candidates, Was 49ab, was observed in detail by Moran et al. (1992), who discussed the possibility of cross-ionization.

Parallel scientific issues – lifetime of AGN luminous episodes and the solid angle over which ionizing radiation escapes – have been addressed for QSOs by seeking changes in the ionization level implied by absorption lines from dense parts of the intergalactic medium (IGM), above all the H I and He II Lyman α forests (Furlanetto & Lidz 2011). A local source of hard radiation, above the mean background at a QSO's redshift, decreases the strength of these absorption features within a radius depending on the local AGN flux. This has been measured as the proximity effect – originally in the spectrum of the QSOs themselves, with redshift mapping to distance in front of the AGN, and later in the transverse proximity effect (Adelberger 2004; Schirber et al. 2004; Gonçalves, Steidel & Pettini 2008; Kirkman & Tytler 2008), as the line of sight to the AGN observed passes close to a foreground AGN. Mismatch between these two kinds of proximity effect could result from episodic luminous AGN phases (Visbal & Croft 2008) or anisotropic escape of the ionizing radiation.

Our approach complements studies of both proximity effects; close companion galaxies can probe smaller separations and lower AGN luminosities than are feasible with the usually statistical nature of absorption-line studies. We rely on an analogous process: detection of ionization in excess of what sources other than the AGN can produce, in this case through changes in emission-line ratios as the AGN contribution becomes comparable to, or exceeds, that from star formation in a companion galaxy.

We have conducted an extensive search for AGN cross-ionization candidates. In Section 2 we describe our sample selection, with participation from Galaxy Zoo volunteers, the choice of observational priorities among these based on physical properties, narrowband imaging of a subset, and spectroscopic observations. In Section 3 we identify a set of candidates for cross-ionization between AGN and companion galaxies, as well as noting instances both of AGN potentially missed in the most common diagnostics due to low gas metallicity, and of close companions showing no influence by luminous AGN. Finally, we compare our subsets of AGN companions with and without spectroscopic evidence of cross-ionization. In quoting luminosities and sizes, we adopt $H_0 = 70$ km s^{-1} Mpc^{-1} and flat geometry.

2 SAMPLE SELECTION AND OBSERVATIONS

2.1 Sample criteria

For detectable cross-ionization of the ISM in a companion galaxy, both the impinging intensity of ionizing radiation from the AGN and the chances of the companion intercepting the pattern of emerging radiation (i.e. ionization cones) are relevant. Our criteria are shown schematically in Fig. 1. Here, r is the projected distance from the AGN to the centre of the companion, and θ is the angle the companion subtends in projection around the AGN. These are largely independent criteria (although for constant galaxy size, larger θ occurs at small r), and we consider both in selecting the most promising targets. Galaxy size is not well-defined, particularly when images overlap so that standard photometric procedures may not separate galaxies properly; operationally we take the extent detected in composite images from the Sloan Digital Sky Survey (SDSS; Abazajian et al. 2009; Alam et al. 2015) for a consistent way to compare different systems. Examination of a variety of our systems shows that this extends to a projected distance from the nucleus roughly equal to the SDSS quantity *petroR90_r*, and about 1.3 times the Petrosian radius *petroRad_r*.
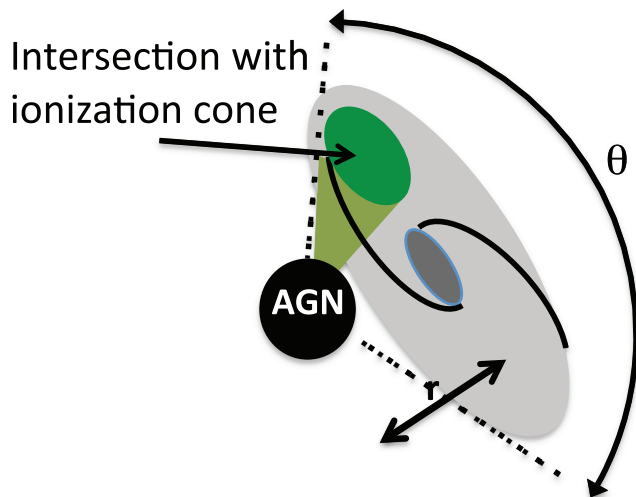
Figure 1. Schematic diagram of an AGN illuminating a large companion galaxy, showing the selection parameters r and θ. The projected separation r, combined with the AGN luminosity, predicts the strength of ionization expected at the companion, while its angular extent θ with respect to the AGN predicts the probability of ionization cones actually intersecting the companion galaxy. Both r and θ are subject to projection effects.

Observed ionization cones have projected full opening angles of typically $70°$ (Wilson 1996; Keel et al. 2012a), half-angle $\approx 35°$. Ignoring projection effects that are poorly known for most objects, this implies that ionizing radiation emerges over a fraction $(1 - \cos 35° = 0.18)$ of the sky around a typical AGN, and suggests that we could expect roughly this fraction of companions to show cross-ionization if they are close enough for the incident AGN radiation to be suitably intense. This is a very crude estimate, since there is such a wide range of observed opening angles and projection factors will enter, but helps to guide our expectations.

Both r and θ are subject to projection effects due to the (essentially unknown) line-of-sight separation between the galaxy centres. Since there is no control over these factors in sample selection, we simply take the observed quantities. However, it may be of interest to estimate the expected projection factors for galaxy separation, and hence in ambient AGN flux predicted based on this separation, for companion galaxies. For this purpose, we carried out a simple Monte Carlo simulation based the slope ζ of the galaxy–galaxy correlation function slope (which is consistent across the separations of galaxy pairs and groups), using a cut in projected radius (whose value is arbitrary since the correlation function is a power law) to model the selection of a sample on projected separation. Using 10^4 Monte Carlo trials for pairs of points separating according to $\zeta \propto r^{-1.6}$, the mean projection effect is poorly defined because of the long tail of widely separated galaxies, but the median projection factor between projected and physical radii is stable at 1.52 (decreasing the inferred intensity of incident AGN radiation by a factor of 2.3).

Ideally, we would seek companion galaxies with the rare combination of being rich in neutral gas to trace ionizing radiation, and poor in ongoing star formation that dilutes the emission lines of AGN-ionized gas. A selection on companion optical colours could eliminate 'red and dead' systems on the red sequence that are very gas-poor, but this could also, in principle, eliminate some galaxies with enough gas for observable line emission if they have low rates

of star formation (or, for example, H I clouds on the periphery of quiescent galaxies).

When both galaxy redshifts are known, we can filter many line-of-sight projections from candidates for genuine companion galaxies. We required $cz < 400$ km s^{-1} to reject line-of-sight companions that are not physically associated; as it turned out, a smaller Δv threshold would have given virtually the same selection. Among all pairs we observed spectroscopically, the median cz is 93 km s^{-1}. All objects we observed with tidal disturbances have component redshifts matching within our selection threshold.

2.2 Sample construction

We compiled a finding list of AGNs with companion galaxies based on the redshift and geometric criteria in Section 2.1, largely through the efforts of volunteer participants in the Galaxy Zoo project (Lintott et al. 2008). A post on the project forum setting out the desired kinds of galaxy pairs led to responses beginning both from objects seen in the normal course of classification for Galaxy Zoo and from SQL queries of the SDSS photometric and spectroscopic catalogs.[1] This initial query selected object pairs projected within 15 arcsec with both redshifts in SDSS DR8, where one had an AGN spectroscopic class and the other had a non-AGN galaxy spectroscopic class. The cut-off in projected separation corresponds to 17.5 kpc at the median sample redshift $z = 0.060$. To this we added additional pairs found by Galaxy Zoo volunteers that satisfied the same criteria except for not having both redshifts available from the SDSS, or fulfilling the linear separation criterion at lower redshifts. In some cases the missing redshift had been measured and was available from sources referenced in NED, and in others, tidal structure made physical association between the galaxies virtually certain (which was confirmed by our spectroscopy). Similarly, we also included nearby systems passing these tests, previously known outside the SDSS imaging region (i.e. Keel 1996 building on the catalogue by Lipovetsky, Neizvestny & Neizvestnaya 1988): NGC 2992, NGC 6786, Kaz 63, and Kaz 199.

This set of pairs was further refined by our inspection of spectra to confirm the clear presence of a spectroscopic AGN. We required a Seyfert nucleus; originally we started compiling LINER AGN as well, but as their inferred ionizing luminosities all fell below our threshold for observation, we ceased collecting them for this program. When only the AGN redshift is known, tidal distortion was taken as secondary evidence that two galaxies are physically associated. These factors led us to a finding list of 212 AGN/companion pairs (Appendix A), incorporating Galaxy Zoo forum postings between 2012 January 16 and 2014 March 15.

From this finding list of 212 AGN/companion pairs, we used large θ and small r as in Fig. 1 to prioritize them for spectroscopic observations. We estimate the ionizing luminosity based on the nuclear [O III] flux. We use [O III] rather than Hα or Hβ, since the broad-line components can suffer obscuration in at least some Sy 2 nuclei; the [O III] luminosity is a nearly isotropic luminosity indicator based on its relation to mid- and far-IR selection (e.g. Keel et al. 1994). The [O III] fluxes are taken mainly from the SDSS spectra, augmented where necessary by published data from other sources. We used these values only in a relative sense here, for ranking priorities; a conversion to absolute values is needed to predict individual values and ask what threshold in ionizing flux should lead to

---

[1] http://www.galaxyzooforum.org/index.php?topic = 279841.210

Table 1. Spectroscopic observations.

UT Date	Galaxies observed
2013 Jan 15	0057+0120,0848+3515
2013 Jan 16	0029+0010,0848+3515, 1214+2931
2013 Jan 17	0029+0010 compn,0757+3511,0848+3515,1200+147
2013 Jan 18	0057+0120,0841+0101,0905+3237,1010+0612,1352+2528
2013 Mar 10	0838+0407,0847+3445,0904+5536,1138+1412,1201-0153,1303-0306,1354+1327
2013 Mar 11	0904+5536,1213+5138,1243+3738,1342+1839,1347+1734,1354+1327
2013 Mar 12	1050+2329,1219+1326, 1414-0000
2013 Mar 13	1042+0502,1101+1017,1132+5257,1142+3251, Kaz 199
2014 Feb 4	0839+4707, UGC 6081, NGC 5279
2014 Feb 5	0838+0407, UGC 6081,NGC 5279
2015 April 23	0848+3515, 1354+1327, NGC 3341, Was 49, NGC 5279
2015 April 24	NGC 3341, 1354+1327
2015 April 26	1201-0153, NGC 3341, NGC 5279, UGC 6081, Was 49

observable ionization consequences. For this, we used the conversion between [O III] and bolometric luminosity from Heckman et al. (2004), namely a ratio of 3500 between bolometric and observed [O III] output, and the mean radio-quiet spectral energy distribution (SED) from the QED project (Elvis et al. 1994), where the ionizing luminosity is about 0.14 of the bolometric value. These give predictions of the incident ionizing flux F_{ion} on companion galaxies from the AGN [O III] flux and companion geometry, which can suggest likely ionization parameters for a particular ISM density. This estimate applies to the projected location of the companion nucleus; in some systems the range between near and far sides of a companion disc is very large. The diffuse phase of the ISM is important here; at its typically low density, relatively few AGN photons will suffice to shift its ionization balance, in contrast to H II regions with higher densities of both particles and stellar ionizing photons. The contributions of these phases differ considerably among galaxies. For this reason, we use the expected ionizing flux from AGN at companion locations only as a relative guide to prioritize our observations.

For each spectroscopic observing session, we selected accessible pairs with either the highest predicted ionizing flux at the companion, or close pairs with the largest projected angle θ spanned by the companion (translated to expected solid angle spanned by the companion as seen from the AGN). Selection for highest incident ionizing flux will restrict this study to luminous AGN in galaxy pairs; these will be a small subset, given evidence that AGN in dense environments (including close pairs) are predominantly of low luminosity (Martínez et al. 2010; Bitsakis et al. 2015), with additional differences between interacting pairs and dense compact groups (Sabater, Best & Argudo-Fernández 2013). Furthermore, AGNs that remain at low luminosity for long periods are unlikely to be able to produce radiatively driven outflows that could contribute to extended emission (Elitzur & Shlosman 2006).

When the companion spectrum is available (from SDSS or other sources as listed by NED), we omitted those with strong line emission from star formation, since weaker contributions from AGN-ionized gas become progressively more difficult to distinguish in composite systems. Previous dual-AGN candidates were retained in our list, since some of these may be instances of cross-ionization where the nucleus and surrounding ISM are blended in the SDSS spectrum (Liu et al. 2011). We note in discussing individual candidates below where a second AGN is clearly present, and how its luminosity affects the likelihood of cross-ionization from the brighter AGN.

Mkn 177 and its close, compact companion object fit our selection criteria, but Koss et al. (2014) find no resolved line emission around the putative AGN, whose long-term variability suggests that it may instead be a very luminous, unusual variable star, or more speculatively, an ejected supermassive black hole leaving the site of interaction.

2.3 Observations: long-slit spectra

Cross-ionization should give spectroscopic signatures such as extended ionized gas with AGN-like line ratios across the companion, and ionization behaviour not symmetric about the companion nucleus. We have carried out a spectroscopic study of candidate AGN in galaxy pairs to isolate a subset with these features.

We obtained spectra of 32 candidate pairs, some multiple times for confirmation or at different position angles, using the Kast double spectrograph (Miller & Stone 1992) at the 3-m Shane telescope of Lick Observatory during 13 nights from 2013 to 2015. For each session, the D46 dichroic beamsplitter separated light into blue and red optical paths, with a nominal split centred at 4600 Å. The wavelength settings were roughly 3400–4600 Å in the blue side and 4600–7400 Å on the red side. The slit width was 2.0 arcsec. Flux calibration used observations of 1–3 standard stars per night. Clouds prohibited observing standards on 2015 April 23, so we used the response curve derived for April 26, and scaled line fluxes in the case of SDSS 1354+1327 to match earlier data where the slits crossed at the nucleus. Observations on each night are listed in Table 1, and descriptions of the spectral characteristics of spatially resolved, extended line emission are given in Table 2. The initial slit orientation crossed both galaxy nuclei, unless SDSS images suggested strong off-nuclear line emission (in tidal tails) via unusual *gri* colours, with further slit orientations in some cases when suggested by system structure or results of a first observation. The data-reduction pathway includes bias subtraction, flat-field correction, resampling to linear wavelength scales, sky subtraction, and flux calibration using nightly standard-star data; these were done using tasks from the IRAF (Tody 1986) *twodspec* package.

The NGC 5278/9 system was also observed on 2018 February 10 in the long-slit mode of the SCORPIO-2 multimode focal reducer (Afanasiev & Moiseev 2011) at the prime focus of the 6-m telescope (BTA) of the Special Astrophysical Observatory, Russian Academy of Sciences. The slit width was 1 arcsec, and the spectral coverage was about 3500–7200 Å with a typical resolution ∼5 Å . Slit positions and orientations were selected to include some of the near-radial emission-line features outside the galaxy discs, through NGC 5278 at PA 100° and NGC 5279 at PA 91°. Each slit position was observed for 3600 s. After standard reduction, the BTA spectra

Table 2. Spectroscopic summary.

AGNs	Type	z	PA°	Description
Candidate cross-ionization systems				
SDSS J002944.89+001011.1	Sy 2	0.0598	49	Line emission extended across pair. Compn [O III]/Hβ drops to ≈ 2.5 (UM 246)
SDSS J005754.03+012013.8	Sy 2	0.0567	168	UM 293. Extended high-ionization emission from AGN to companion
SDSS J083902.96+470756.3	Sy 2	0.0524	56	Extended high-ionization emission
SDSS J084810.11+351534.3	Sy 2	0.0573	72, 107	KUG 0845+354. 2nd Sy 2 or cross-ionization, AGN line ratios across extended region
SDSS J104232.05+050241.9	Sy 2	0.0272	98, 212	NGC 3341. Extended emission into companion
SDSS J110019.10+100250.7	Sy 2	0.0361	133, 134	UGC 6081; 2 AGNs, AGN-ionized cloud
SDSS J120149.74-015327.5	Sy 1	0.0907	139,142	AGN is Sy 1.9, ionized tail opposite star-forming companion
SDSS J121418.25+293146.7	Sy 2	0.0632	60, 147	Was 49; 2nd AGN or cross-ionization
SDSS J134143.75+554025.5	Sy 2	0.0251	98	NGC 5278/9; 2 AGNs, high [O III]/Hβ, He II in filaments
SDSS J135429.05+132757.2	Sy 2	0.0633	84, 186, 194	Both galaxies have similar line ratios; [O III] in tail opposite companion
Other systems:				
SDSS J075729.04+351105.9	Sy 2	0.1117	99	Double spatial/spectral line profiles
SDSS J080004.05+232616.2	Sy 2	0.0292	118	Velocity structure in small emission region around AGN
SDSS J083848.14+040734.0	Sy 2	0.0476	96	AGN emission extended 5 arcsec toward H II compn
SDSS J084135.08+010156.2	Sy 2	0.1106	48	Two AGN, extended [O III] beyond each
SDSS J084742.44+344504.4	QSO	0.0640	20	PG 0844+349. Companion has resolved rotation curve, lacks [O III]
SDSS J090436.92+553602.9	Sy 1	0.0372	7	Emission around AGN extended by 15 arcsec more toward absorption-ine companion
SDSS J101043.36+061201.4	Sy 1	0.0978	58	[O III] resolved over 8 arcsec. Weak emission in companion, no [O III]
SDSS J105030.47+232931.4	Sy 1.8	0.0604	117	AGN unresolved. Star-forming companion
SDSS J110157.90+101739.3	Sy 1.5	0.0341	138	Extended rotation curve over 29 arcsec star-forming line ratios
SDSS J113240.25+525701.3	Sy 2	0.0266	75	Mkn 176. AGN emission extended to 6 arcsec opposite from 2 companions
SDSS J113858.89+141253.2	Sy 2	0.0805	10	Companion has resolved line emission, star-forming ratios
SDSS J114252.83+325124.2	Sy 2	0.0666	165	Companion has extended emission, star-forming ratios
SDSS J120041.39+314746.2	Sy 2	0.1159	33	AGN emission spans 14 arcsec blends w/companion
SDSS J121303.34+513854.9	Sy 2	0.0849	118	AGN unresolved. Star-forming companion emission resolved
SDSS J121943.13+132659.9	Sy 2	0.0647	50	AGN em unresolved, companion has [N II] and Balmer absorption
SDSS J124322.55+373858.0	Sy 2	0.0859	120	LINER-like AGN em to 8 arcsec opposite star-forming companion
SDSS J130354.71-030631.8	Sy 2	0.0778	166	AGN emission not well resolved
SDSS J134203.48+183901.5	Sy 1.8	0.0845	102	AGN em (low-ion NLR) to 8 arcsec opposite star-forming companion
SDSS J134736.39+173404.6	Sy 2	0.0447	108	AGN-ionized knot at 18 arcsec opposite star-forming companion
SDSS J135255.67+252859.6	Sy 1.5	0.0636	176	Strong lines like starbursts, but He II/H$\beta \approx 0.2$ and broad Hα
SDSS J141447.15-000013.1	Sy 2	0.0475	65	Sy 2 plus transition nucleus w/[O III]/H$\alpha \approx 2$. Emission unresolved
Kaz 199	—	0.0155	5, 54	NGC 6636. [O I]/H$\alpha \approx 0.03$, may not be AGN

were flux-calibrated using a standard star observed on the same night. These data were obtained using 1×2-pixel binning during readout, for a scale of 0.356 arcsec per pixel along the slit, which we summed by a further factor of 3 to get sets of line measures every 1.07 along the slit. This provides enough surface-brightness sensitivity to detect He II λ4686 emission in some of the extended features at levels indicating AGN photoionization, independent of issues with the stronger line ratios at low metallicity.

We estimate errors on the emission-line ratios measured in our spectra using the same Gaussian-fitting procedure as used to derive their radial velocity and fluxes, the deblending option in the IRAF routine *splot*. This was done by adding an emission-line position at an arbitrary wavelength where no line is expected, in the red and blue regions, and adopting the flux statistics of the resulting fictitious lines as the error distribution. We examined the behaviour of this error distribution with local flux, finding no significant trend (i.e. the effects of Poisson noise from the galaxy continuum are weak) in the Lick spectra. The deeper BTA spectra do show an error increasing with line flux, so we include this factor for the BTA spectra. These estimated errors are propagated into the emission-line ratios used to infer ionizing mechanisms.

To assess the dominant ionizing mechanism in our spectra, we rely on the approach pioneered by Baldwin, Phillips & Terlevich (1981), widely known as BPT diagrams. In particular, star-forming objects and AGNs are generally well separated in a diagram comparing the ratios of strong emission lines [O III] λ5007/Hβ and [N II] λ6583/Hα. Specifically, we use the updated boundaries specified by Kewley et al. (2006). This single diagram, while relying on the spectral lines most easily detected in the optical, can become ambiguous at low metal abundances (as in some of the EELRs examined by Keel et al. 2012a). He II or [Ne V], when seen over large areas, are virtually certain indicators of photoionization by AGN radiation, but our data are only rarely sensitive enough to reveal these in the outskirts of the galaxies. Further, the wavelength range around He II λ4686 at redshifts $z = 0.02-0.04$ (typical of the bright objects in this sample) is compromised by a night-sky emission line in spectra from Lick Observatory.

Of the 32 systems we observed, 10 show evidence of extended AGN-ionized gas in companion galaxies or tidal tails. The long-slit results for the 10 objects with possible AGN ionization in the companion galaxies (or tidal tails) are presented in Fig. 2. Spectral properties were evaluated using Gaussian fits to 2-pixel (1.5 for Lick data) or 3-pixel (1.07 for BTA data) sums along the slit. The
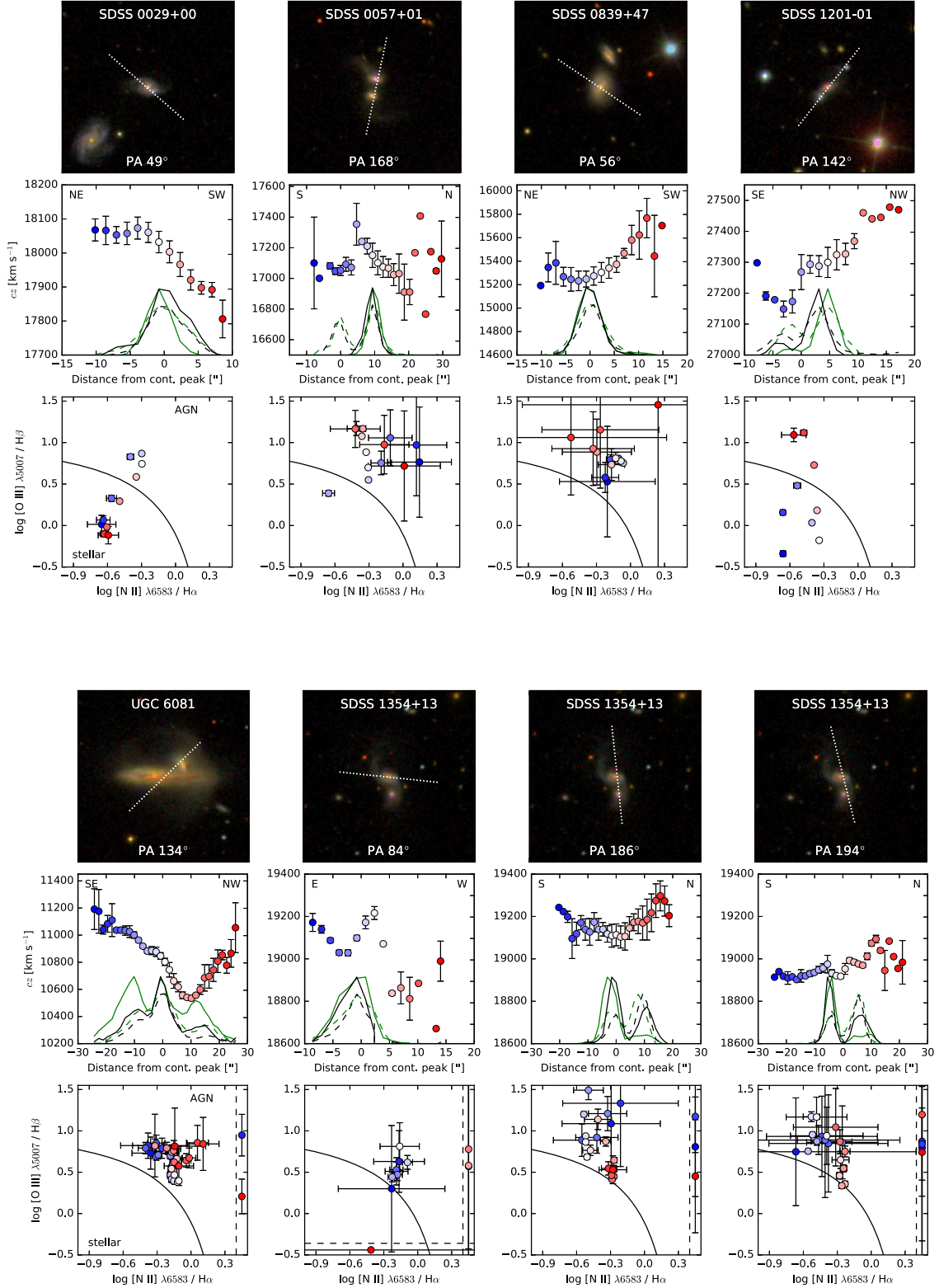
Figure 2. Results of long-slit spectroscopy of candidate AGN cross-ionization systems. For each object, the top panel shows the slit position on an SDSS DR12 *gri* composite image spanning 100 × 100 arcsec. The middle panel shows the heliocentric radial-velocity profile along the slit, with error bars based on agreement among multiple lines measured at each position, and colour coding of points to indicate position. Below the velocity profiles are intensity traces of Hα (black) and [O III] (green, full lines), with the adjacent continuum (dashed in matching colour) for each, on arbitrary linear vertical scales, to show the alignment between intensity and velocity features. The bottom panels show the strong-line BPT classification diagram with the starburst/AGN dividing curve from Kewley et al. (2006); point colors here show where along the slit AGN-ionized regions occur in comparison with the middle panels. The Hβ flux was estimated from Hα and an intrinsic Balmer decrement 2.85; additional reddening correction would move data points upward and toward (or further into) the AGN-ionized region above the curves. Regions appear in this panel only if Hα, [O III] and [N II] are all detected.

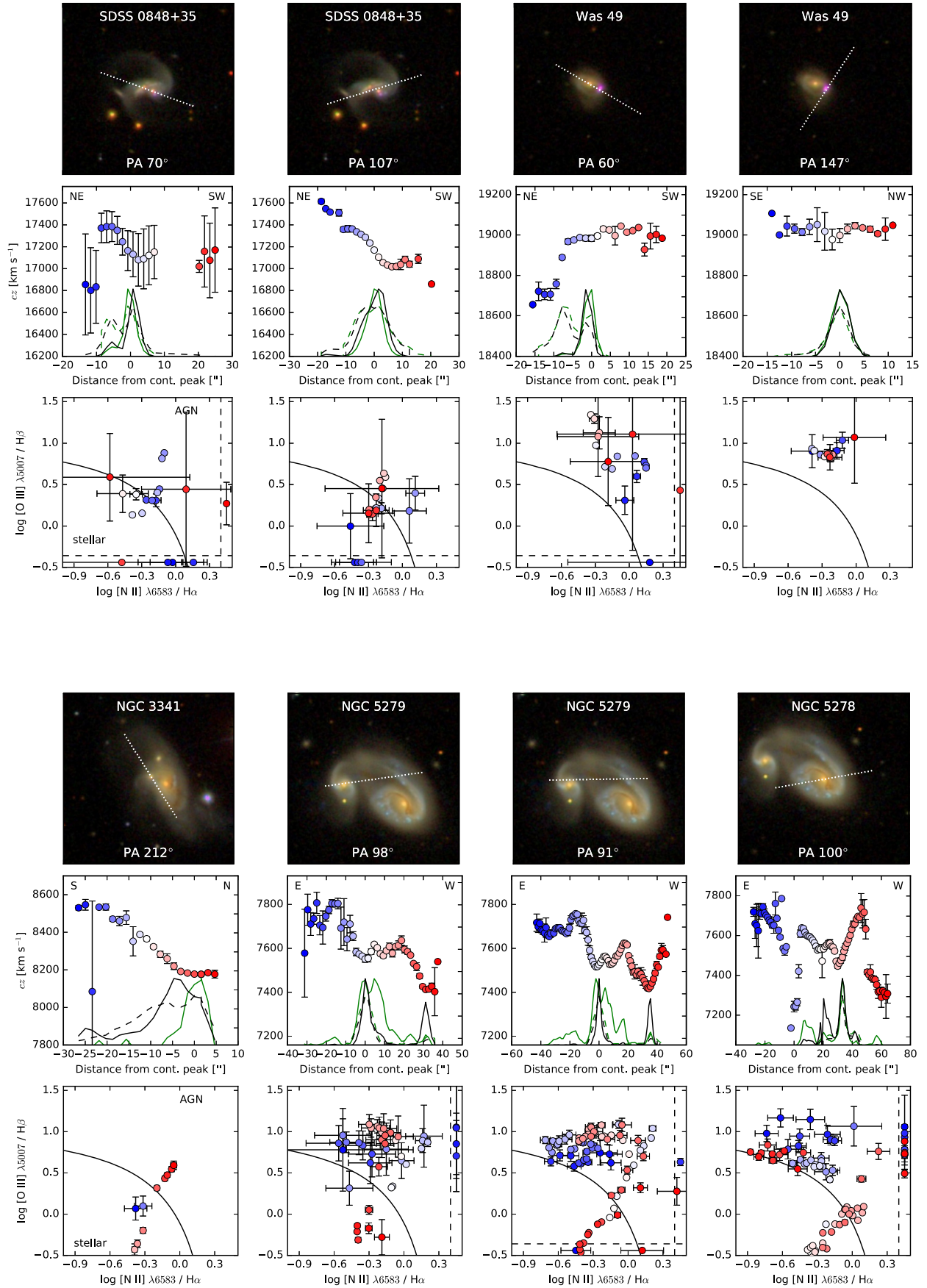**Figure 2** – *continued*

Table 3. Narrowband imaging.

Object	z	Bands	Exposure [min]	Telescope	UT date
Kaz 199	0.0155	V/510	20/30	SARA-KP	2012 Feb 25
Kaz 199	0.0155	V/514	10/30	KPNO 2.1m	2013 Apr 13
Kaz 199	0.0155	R/6653	10/45	KPNO 2.1m	2012 May 29
Mkn 176	0.0274	V/510	20/60	SARA-KP	2013 Mar 12
NGC 2992	0.0077	V/510	15/120	SARA-KP	2013 Feb 2
NGC 3341	0.0273	V/510	30/120	SARA-KP	2013 Feb 2
NGC 3341	0.0273	V/510	20/60	SARA-KP	2014 Dec 29
NGC 3341	0.0273	B/V	30/30	SARA-JKT	2017 Feb 4
NGC 3786	0.0089	V/510	20/60	SARA-KP	2013 Apr 4
NGC 5278/9	0.0251	6000/6693	10/20	KPNO 2.1m	1985 May 18
NGC 5278/9	0.0251	V/510	10/60	SARA-KP	2015 Mar 27
UGC 3995	0.0158	V/510	20/60	SARA-KP	2013 Dec 31
UGC 6081	0.0361	Hα/continuum	33/33	CMO 2.5m	2018 Apr 16
UGC 6081	0.0361	[O III]/continuum	33/33	SAI 2.5m	2018 Apr 16

top panels show the slit locations in these systems superimposed on composite SDSS *gri* images. The middle panel for each spectrum shows the redshift behaviour (heliocentric *cz*) along the slit as well as intensity slices in [O III], Hα, and their adjacent continuum regions. The bottom panels show the strong-line BPT diagram with the star-forming/AGN boundary from Kewley et al. 2006; the colours of points match between the velocity plots and BPT diagrams to show where the AGN-ionized regions occur along the slit. The effects of underlying stellar absorption drive us to estimate Hβ from Hα, since the absorption correction is both smaller and less variable with stellar population for Hα. The greater strength of Hα further reduces this effect, and the equivalent widths are small enough in many instances to make the uncertain absorption correction relatively large in spectra with insufficient signal-to-noise to model the local stellar populations. We therefore estimate the flux of Hβ from that of (narrow-line components of) Hα and a Balmer decrement of 2.85. A key virtue of the BPT diagram is that it is almost completely reddening-independent. However, using Hα data to estimate Hβ, as we do, introduces a reddening dependence, in the sense that [O III]/Hβ will be underestimated in reddened systems, since the standard Balmer decrement will lead to an overestimate of the Hβ flux. We can tolerate this effect, since in all parts of the strong-line BPT diagram, reddening correction will move data points further into the AGN region. This approach is thus conservative with regard to identifying AGN-photonized regions.

The strong-line BPT diagrams, while allowing examination of the most extensive areas, may be misleading when low-metallicity gas is involved, such as is encountered in tidal debris and the outer discs of spirals (Groves, Heckman & Kauffmann 2006; Kawasaki et al. 2017). AGN photoionization models with varying abundances (oxygen and nitrogen having the strongest signatures) show that nitrogen abundances below solar can move AGN-ionized gas into parts of the usual BPT diagrams occupied by star-forming regions (Storchi-Bergmann et al. 1998; Castro et al. 2017); in particular, [N II] and [S II] weaken at fixed [O III]/Hβ. So, while AGN-ionized gas may be securely identified if its strong-line ratios place it in the 'AGN' region of the BPT diagrams, lower-metallicity counterparts may require additional information for secure classification. Significant He II or [Ne V] emission can play such a role, but these lines are comparatively weak in AGN narrow-line regions, and would not be detected outside the nuclei in most of our Lick spectra. The [O I] λ6300 line is detected in some of our spectra and can help resolve this ambiguity, since this line is very weak in normal H II regions.

An additional ionizing process – shocks – is found to be important around the jets and in high-velocity outflows of AGN, particularly radio-loud AGN. Recognizing their role has proven to be subtle from only the strong optical emission lines. When the Baldwin et al. (1981) classification was initially formulated, what became known as LINERs were broadly identified as shock-ionized. As additional data have accumulated, showing that some LINERs are indeed photoionized by AGN (at lower ionization parameters than Seyfert nuclei) while others represent shocked gas in merging systems, and still others are photoionized by hot evolved stars (Stasińska et al. 2008; Johansson et al. 2016), integrated strong-line ratios by themselves are seen to give little discrimination on this question. Weaker lines, especially [O III] λ4363 and [O I] λ6300, provide more diagnostic power (but are not uniformly detected in the extended clouds in our data). On the broader question of separating LINERs from Seyfert nuclei, Kewley et al. (2006) find that either [S II]/Hα or [O I]/Hα gives more consistent results than [N II]/Hα when compared to [O III]/Hβ (the 'standard' strong-line diagram). However, especially at lower metallicity, these more diagnostic lines become weak and their use becomes less powerful. Pending data of higher signal-to-noise ratio, we note that important shock contributions around AGNs are largely associated with radio-loud objects, which are relatively rare both in the overall AGN population and in our sample.

In addition to line ratios, one might often (although not always) expect kinematic disturbances or broad lines where shock ionization is important. In the extended emission regions in our sample, we do not see any lines with the typical FWHM $> 300 \, \mathrm{km \, s^{-1}}$ or velocity jumps of similar amplitude that are comparable to the shock velocities needed to give the observed excitation level in [O III]/Hβ.

2.4 Observations: narrowband imaging

Our spectroscopy is supplemented by narrowband imaging for eight systems, summarized in Table 3. For seven of the objects with the highest priority for spectroscopic observations in the redshift range $z = 0.008 - 0.027$, where [O III] falls in the band of an available filter, we obtained images in redshifted [O III] and the *V*-band continuum using the SARA 1-m remote telescope at Kitt Peak, Arizona, and the 1-m Jacobus Kapteyn telescope at La Palma, now operated by SARA (Keel et al. 2017a). Narrowband exposures in a filter of 100-Å FWHM were 1–2 h total, with 15–30 min in *V*. Among these, we recover the well-known ionization cones in NGC 2992 (Wehrle & Morris 1988; Allen et al. 1999; Veilleux, Shopbell & Miller 2001)
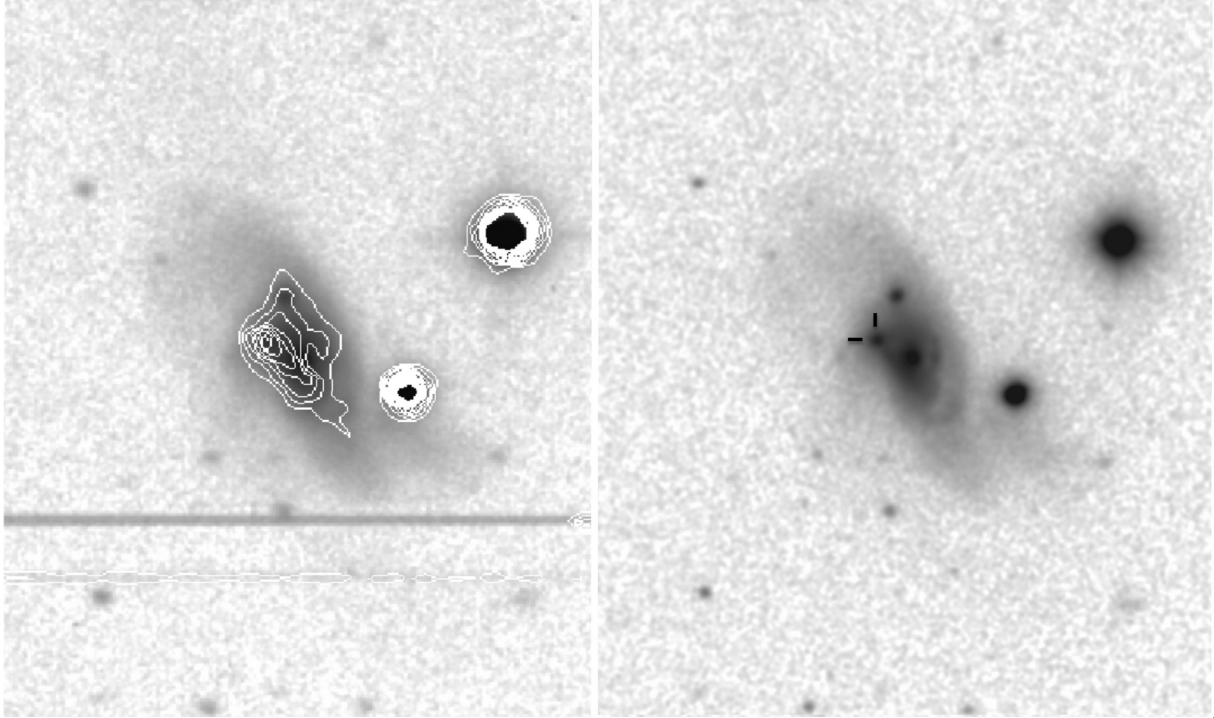
Figure 3. [O III] structure (linearly spaced contours) superimposed on the matched-resolution *V*-band continuum of NGC 3341, with a higher-resolution *V* image from the JKT also shown for comparison of the inner structure. The Seyfert nucleus in this system is in the small companion galaxy to the east (indicated by tick marks in the right-hand panel); the [O III] structure may represent an ionization cone composed of material mainly in the disc of the large galaxy. Stellar residuals result from colour differences between foreground stars and the galaxies; two bright-star charge trails are seen on the southern side. The area shown is 167×201 arcsec, with north at the top. The intensity mapping in *V* uses a logarithmic scale offset from zero to avoid amplifying noise around the sky level.

perpendicular to its disc plane (but not oriented toward either its tidal tail or companion). We find only nuclear emission from Mkn 176. NGC 3786/8 and UGC 3995 A/B show [O III] emission only from the nuclei and knots in the spiral arms, as is typical for spirals. On this basis, we did not obtain new long-slit spectroscopy of Mkn 176, NGC 2992, NGC 3788, or UGC 3995.

NGC 3341 shows a potential morphological signature of cross-ionization. The AGN here is in a small galaxy projected against the disc of a much larger spiral. In [O III], there is a triangular region of emission crossing the large disc at a skew angle with its apex at the AGN (Fig. 3), which we tentatively interpret as an ionization cone of gas in the large galaxy. The slit location for spectroscopy was selected to sample this region, rather than crossing the nucleus of the large companion galaxy.

Motivated by extended [O III] structure in our SARA images of Kaz 199, we obtained more detailed images with the KPNO 2.1-m telescope. [O III] was isolated with a filter of 174 Å FWHM centred at 5142 Å and Hα with a filter of 68 Å FWHM centred at 6653. *V* and *R* were used for continuum subtraction.

For NGC 5278/9, we also analyse the Hα and continuum images from the KPNO 2.1-m telescope described by Kennicutt et al. (1987), which guided our slit placement on noting that this pair was included in the AGN/companion sample. Our spectroscopic data, designed to encompass three of these near-radial filaments, help interpret the nature of the emission filaments mentioned by Keel et al. (1989). Additional images in [O III] were obtained with the SARA system.

Emission-line mapping of UGC 6081 was carried out on 2018 April 16 at the 2.5-m telescope of the Sternberg Astronomical Institute (SAI) of the Caucasus Mountain Observatory (CMO) on Mt.

Shatdzhatmaz (Kornilov et al. 2014) with the Mapper of Narrow Galaxy Lines (MaNGaL). MaNGaL (Moiseev & Perepelitsyn, in preparation) is a tunable–filter imager based on a scanning Fabry-Perot interferometer with low interference order.[2] The peak of filter transmission (FWHM≈15Å) was centred on the wavelength corresponding to the redshifted [OIII]λ5007 and Hα emission lines. Continuum images were consecutively exposed at wavelengths shifted by ∼50 Å and subtracted to produce net emission-line images.

For galaxies or regions with large enough equivalent width in the [O III] lines, we can produce [O III] images from linear combinations of the SDSS survey images (as shown by Keel et al. 2012a, and addressed systematically by Sun et al. 2018). We do this for Was 49 (Fig. 5), revealing extensions from the AGN in opposite directions, possibly including gas in the large companion disc.

3 CROSS-IONIZATION (AND MISSING-IONIZATION) CANDIDATE SYSTEMS

Several of the systems in Table 2 show evidence of cross-ionization. Others show no such evidence despite high *a priori* odds of seeing it from the system properties. We discuss some of their individual properties here.

SDSS 0029+00 (UM 246): A second spectrum of the companion galaxy to the south shows a potential AGN signature on the northern side of its disc. The spectrum crossing the AGN itself shown in Fig. 2

Table 4. Recombination-balance analysis.

Quantity	NGC 5278	NGC 5279	UGC 6081 SE	UGC 6081 NW
Hα flux, nucleus (er g cm^{-2} s^{-1})	2.17×10^{-15}	2.20×10^{-15}	5.09×10^{-14}	2.86×10^{-13}
[O III] λ5007 flux, nucleus (er g cm^{-2} s^{-1})	9.7×10^{-15}	1.2×10^{-14}	1.6×10^{-14}	1.44×10^{-13}
L(ion) from [O III] (erg s^{-1})	4.9×10^{42}	6.2×10^{42}	9.4×10^{43}	1.9×10^{44}
Q(ion) from [O III] (photons s^{-1})	1.1×10^{53}	1.4×10^{53}	2.2×10^{54}	4.4×10^{54}
F(MIR) (8–25 μm) (er g cm^{-2} s^{-1})	1.5×10^{-11}	8.5×10^{-12}	2.2×10^{-11}	3.0×10^{-11}
L(MIR) (erg s^{-1})	1.5×10^{43}	8.8×10^{42}	6.3×10^{43}	8.6×10^{43}
Max L(ion) (erg s^{-1})	2.0×10^{43}	1.5×10^{43}	1.6×10^{44}	2.8×10^{44}
Extended region needs:				
L(ion) (erg s^{-1})	$>4.2 \times 10^{43}$	$>1.4 \times 10^{43}$	$>9.4 \times 10^{43}$	$>1.9 \times 10^{44}$
3 $\times$ structure correction (erg s^{-1})	1.3×10^{45}	4.2×10^{44}	2.8×10^{44}	5.7×10^{44}

includes tidal arms, whose emission-line ratios indicate a dominant role for local star formation.

SDSS 0057+01 (UM 293): AGN-ionized line ratios extend over most of the region sampled in both galaxies. The outermost parts at both ends of the slit are kinematically distinct from the rotational signature of the AGN host itself.

SDSS 0839+47: Our spectrum across the AGN host shows that the AGN ionizes gas across the galaxy, with increasing ionization in the outer parts. The SDSS spectrum of the companion galaxy shows line ratios indicating star formation, albeit with [O I] rather strong at about $0.07 \times$ Hα, broadly consistent with mixed ionization sources. This system was flagged by Comerford & Greene (2014) for showing velocity asymmetries in both Balmer and forbidden emission lines.

SDSS 1201+01: The companion galaxy shows line ratios indicating ionization by hot stars. Gas in the tidal tail on the opposite side of the Sy 1.9 AGN is photoionized by the AGN.

UGC 6081: This pair has two heavily reddened Sy 2 nuclei and shows AGN ionization along an extent of 58 arcsec (41 kpc). The extended emission might fall in the same category of radial extent >10 kpc as the 'Voorwerpjes' (Keel et al. 2012a), depending on which of the AGN lights it up. We do not have the three-dimensional information to tell which is responsible (if indeed one dominates in the tidal debris seen at large radii). We do have the information for a rough ionization-balance calculation as done above for NGC 5278/9. These nuclei are more luminous and much more heavily reddened than in NGC 5278/9; applying a single foreground-screen reddening correction based on the nuclear Balmer decrements suggests that the NW AGN, in the smaller galaxy (UGC 6081 NED01), is twice as luminous in [O III]. Our estimates (Table 4, listing dereddened values in this system) show that the energy balance makes it plausible for the SE AGN (in UGC 6081 NED02) to power the most distant gas we observe spectroscopically along the slit to its southeast, although whether this works in detail depends critically on the fine structure of the gas (since the peak surface brightness we observe places the strongest limits on the incident flux, and is strongly dependent on image quality). Much of the reddening toward each nucleus may take place close to our line of sight rather than as surrounding 'cocoons' covering large solid angles; the WISE data suggest that in neither one does the MIR component of the SED dominate over ionizing radiation reaching surrounding gas. Using our conservative fine-structure correction (a factor of 3 as noted above), the case for AGN fading in this system is weak (energy shortfall 1.7–2.0 times depending on which AGN is responsible, and no shortfall if both contribute to the ionization of the extended cloud).

The tunable-filter data are compared in Fig. 4. They reveal rich structure around both galaxies, with emission extending 25 arcsec (18 kpc) from both AGNs. The emission regions occur within the tidal debris and loop seen in the starlight continuum, fitting with a common pattern of kinematically quiescent EELRs as photoionized tidal tails. Within the host galaxy discs, Hα dominates over [O III] emission, which is reversed outside the galaxy discs; there are distinct bright knots of higher [O III]/Hα within the extended clouds. The structure we see does not make clear to what extent each AGN contributes to the overall ionization, except that it occurs on only one side of the NW AGN and more symmetrically about the SE one.

SDSS 1354+13: Both galaxies show similar line ratios, marking a possible dual AGN system flagged by Liu et al. (2011) from the SDSS spectrum, and with a velocity asymmetry in the SDSS spectrum noted by Comerford & Greene (2014). AGN-ionized gas is more extended than the starlight continuum, notably in the tidal tail to the south, where it is detected out to a radius of 22 arcsec (27 kpc) along two adjacent slit positions. Comerford et al. (2017) recently presented a suite of spectroscopic data showing both an EELR and a spatially resolved outflow, with implied timescales suggesting recurrent episodes of nuclear activity in which the AGN has turned 'off' and 'on' again within 10^5 yr. Their EELR detection south of the nucleus overlaps with our data along the N–S slit position; our detection extends slightly farther from the AGN. Both their data set and ours indicate that the EELR is part of a tidal tail.

SDSS 0848+35: There is an isolated region of AGN-ionized gas at a projected radius 21 arcsec (23 kpc).

Was 49: Identified in this context by Moran et al. (1992), this may remain the best low-redshift cross-ionization candidate. Detailed study of the AGN by Secrest et al. (2017) stresses its high luminosity and implied black hole mass relative to the very modest stellar mass of the host galaxy. The [O III] structure around the AGN is elongated perpendicular to the line between the galaxies (Fig. 5); the images in Secrest et al. (2017) show that part of this emission is in a single bright discrete source just north-west of the AGN. All the locations along our spectroscopic slits in this pair are AGN-ionized except the nucleus of the large companion galaxy; the AGN emission is largely continuous with the portion of the large galaxy's rotation curve sampled in our data. Integral-field spectroscopy with high angular resolution could show whether the gas seen surrounding the AGN on arcsecond scales kinematically matches either its own radial velocity or the rotation pattern of the larger disc. In the latter case, the ionization pattern in the disc might reflect its intersection with the pattern of escaping ionizing radiation.
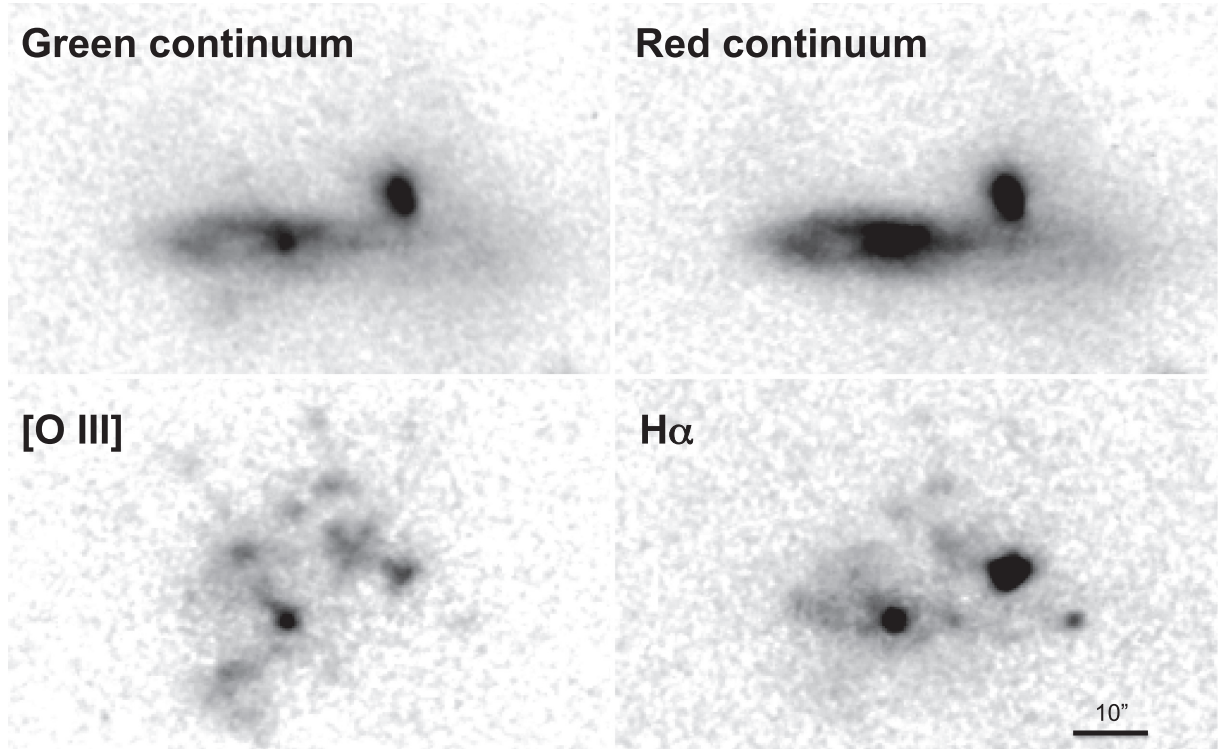
UGC 6081

Figure 4. The SAI 2.5m tunable-filter data for UGC 6081. Continuum images are offset by 50 Å from the redshifted line wavelengths, and bottom images show net line emission after continuum subtraction. North is at the top and east to the left; each panel spans 50×82 arcsec. The nucleus of the southeastern disc is bright in all these bands and gives a convenient reference point for comparison. Emission regions appear projected as far as 25 arcsec from each nucleus, so that even if the nearer one is solely responsible for the photoionization at these locations, the radial extent from the ionizing source is at least 18 kpc. The intensity scales are similar to Sloan image products, changing gradually from linear at low intensities to logarithmic at bright levels.
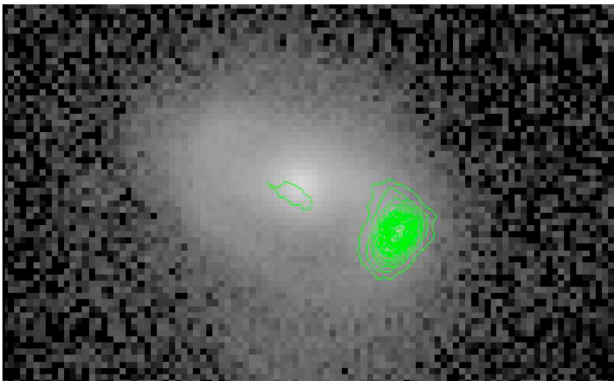

Figure 5. [O III] structure (contours) superimposed on the r-band image of Was 49, from SDSS data using the difference between g and r data to trace line emission. The Seyfert nucleus in this system is in the small companion galaxy to the west, superimposed on the large companion disc and centred in the contours; the [O III] structure may represent an ionization cone The area shown is 26×45 arcsec, with north at the top.

NGC 3341: This pair has nearly the ideal geometry from Fig. 1, with an AGN hosted in a compact galaxy close to a much larger spiral (Barth et al. 2008). In a multiwavelength study, Bianchi et al. (2013) set very low limits on AGN in the other components of this system. Our emission-line imaging (Fig. 3) shows a possible ionization cone in [O III] southward from the AGN across the larger disc. However, the spectroscopic data show AGN ionization dominant only close to the AGN, so this structure may be an accident of the spiral pattern and location of star-forming regions. On the other hand, the spectrum shows unusually strong [O I] emission for pure stellar photoionization across much of this region, with [O I] $\lambda6300$/H$\alpha \approx 0.03$. More detailed data and modeling would be needed to tell whether this is low-metallicity gas ionized by an AGN, a composite of both ionization sources blended along the slit, or something yet more complex.

NGC 5278/9: This pair has two low-luminosity AGNs, near the Sy 2/LINER boundary in line-ratio diagrams depending on aperture size. The system shows extensive filaments or plumes in line emission, some almost radial (Keel et al. 1989, Fig. 6). Our spectroscopy in the BPT diagram shows AGN-ionized gas across the pair, including one of these plumes to the east. This may suggest that the AGNs either are heavily obscured along our line of sight or have faded over the light traveltime from the nucleus to the extended emission regions. Because gas in each disc may be largely shielded from its own AGN, this pair is a potential instance of cross-ionization.

In this system, we have the data to estimate both the nuclear luminosities and the ionizing-flux requirement at various points in the extended emission, to see whether the nuclear output has changed dramatically over the relevant light traveltime, and how important obscuration of the AGN is along our line of sight. Since these nuclei were not observed spectroscopically in the SDSS, we use the optical emission-line data within 4.7 apertures reported by Keel et al. (1985). For mid-infrared nuclear properties, we take the PSF-fitting
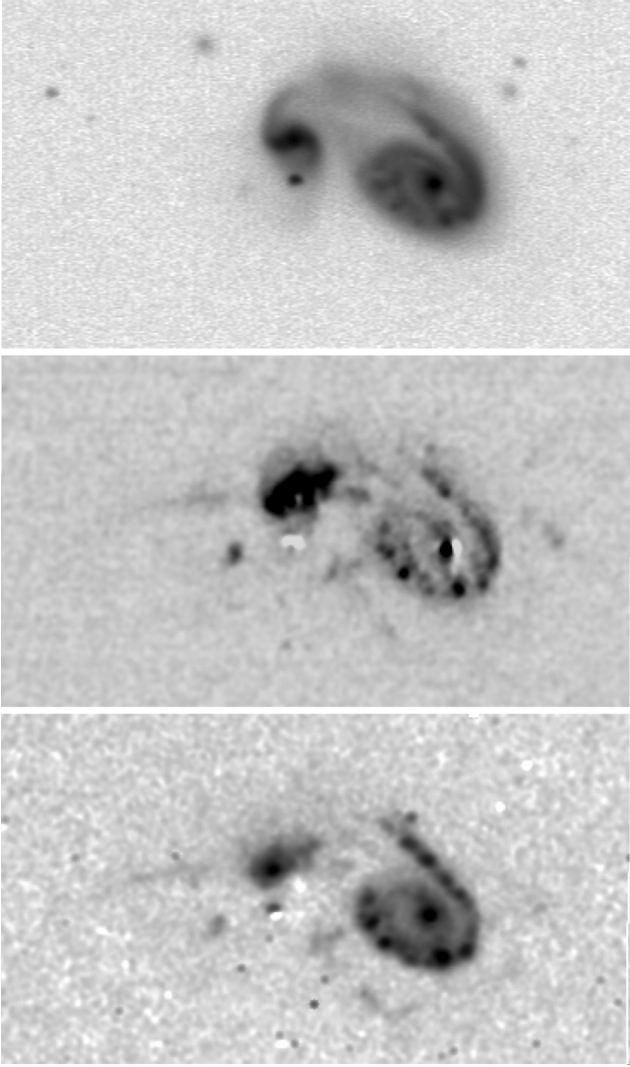
Figure 6. The NGC 5278/9 system in the *V* band (top), continuum-subtracted [O III] (middle), and continuum-subtracted Hα+[N II] (bottom). The field shown is 141 arcsec across with north at the top. PSF mismatches between on-band and continuum images give artefacts at the locations of bright stars and the galaxy nuclei. At least three partly radial emission features are present without significant continuum counterparts; our spectrograph slits crossed the nuclei both of NGC 5279, included much of the emission feature extending to its east, and NGC 5278, covering the two oppositely directed emission filaments to the ESE and WNW. The intensity scales are logarithmic starting at levels slightly offset from zero.

WISE fluxes (Wright et al. 2010), using the 'compromise' spectral slope conversions from Cutri et al. (2012) and bearing in mind the potential non-nuclear contribution within the WISE PSF. Conversion from Hα surface brightness in extended regions to required luminosity in the ionizing continuum followed Keel et al. (2012a). To be conservative, we take the distance from extended cloud regions to each nucleus to be in the plane of the sky, minimizing the ionizing-luminosity requirements. The quantities involved in this comparison are given in Table 4.

This kind of estimate gives only a lower bound to the required ionizing luminosity of the AGN at the relevant time, both because a given parcel of gas is unlikely to be optically thick at the Lyman edge, and because we measure spatially averaged surface brightness in structures that are likely to be very patchy. For example,

Gagne et al. (2014) and Keel et al. (2017b), working at a linear resolution of ≈150 pc from *HST* imaging of the 'Teacup' AGN, find that this calculation for the brightest regions underestimates the ionizing continuum by about a factor of 3 over a wide range in radius. For NGC 5278/9, we average over a yet larger region, roughly 2 kpc in size. Lacking more detailed information on the fine structure in NGC 5278/9, we consider that the multiplication factor will be at least 3. However, with the evidence from He II emission that the extended features from both galaxies are AGN-ionized, a fading scenario would be plausible only if one of the AGNs dominates the ionizing output, since it would be unlikely for both AGNs to have behaviour synchronized at the 10^4-yr level, much faster than dynamical time-scales associated with the galaxy encounter.

The deep BTA spectra, centred on each nucleus and aligned along the near-radial filaments, not only extend the radial range over which we can locate feature on the BPT diagram, but add key new information – in three of these filaments, extending outside the detected stellar discs, the He II/Hβ ratio is so high that it must arise from photoionization by an AGN continuum (Table 5). The regions in NGC 5278 fall near the boundary between stellar and AGN photoionization in the BPT diagram, illustrating the effects of low metallicity as this primarily reduces the strength of [N II].

Among galaxies that our spectroscopic data suggested are pairs of AGNs rather than instances of cross-ionization, *HST* images recently presented by Storchi-Bergmann et al. (2018) indicate that SDSS J084135.04+010156.3 may instead show cross-ionization. Their [O III] and Hα images show that the outer part of the 10-kpc ionization cone from the AGN coincides with the companion galaxy in structure and brightness enhancement, suggesting that at the limited spatial resolution of our data, that emission masquerades as a second AGN.

NGC 6636 = Kaz 199: The small northeastern component of this pair (outside the SDSS footprint) has been catalogued as a Seyfert galaxy. We are unaware of a previously published spectrum of the AGN. In our new data, the strong lines would classify both galaxies as star-forming, but [O I] has intensity ≈0.05 × Hα across a large region, at the very high end of values seen in disc H II regions and potentially a sign of composite ionization sources. In our [O III] images, the small galaxy (with reported AGN) is surrounded by an arc of emission-line knots (Fig. 7), in addition to the region tracing the tidally distorted arms of the larger galaxy. The sizes of these knots are consistent with unresolved H II regions, rather than the filamentary appearance often seen in giant AGN-ionized clouds (Keel et al. 2012a; Keel et al. 2015).

Some systems attract attention because of what we *don't* see. The best example is SDSS J084742.44+344504.4, also catalogued as PG 0844+349, a QSO with a nearby large spiral companion galaxy projected 25 away (32 kpc). Its F_{ion} and projected separation would be very favorable for cross-ionization, but our spectrum shows no evidence of this. Fig. 8 shows the velocity structure of this companion galaxy to the southwest, along its projected major axis. [O III] is detected only at the two positions in its disc where the slit crosses the spiral arms, weaker than Hα, so there is no evidence of external AGN ionization. An *HST* archival image (from program 9763, with Barth as principal investigator) shows this to be a very symmetric, inclined grand-design spiral, similar in scale to the QSO host galaxy itself (Fig. 9). The outer arms are so open in comparison to the inner structure that they may be tidally induced; the dust lanes on the northern side of the arms plus our velocity measurements show that the spiral pattern is trailing. The slit spectroscopy by Hutchings & Crampton (1990) shows only weak emission in the southern

Table 5. Emission-line ratios in extended filaments of NGC 5278/9.

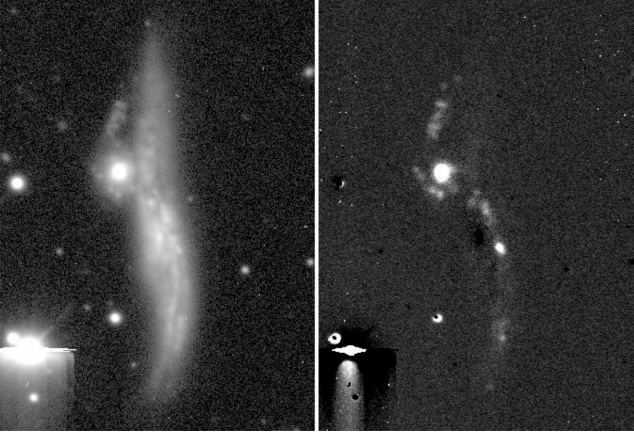| Ratio	NGC 5278, PA 100, 22-29 E	NGC 5278, PA100, 20-27 W	NGC 5278, PA100, 19-28 E
He II λ4686/Hβ	0.24 ± 0.05	0.54 ± 0.15	0.043 ± 0.08
[O III] λ5007/Hβ	4.69 ± 0.25	6.11 ± 0.75	10.69 ± 0.75
[O III] λ5007/Hα	1.44 ± 0.05	1.87 ± 0.08	3.24 ± 0.07
[N II] λ6583/Hα	0.47 ± 0.05	0.18 ± 0.03	0.43 ± 0.03

Figure 7. *V*-band continuum (left) and subtracted [O III] (right) images of Kaz 199 = NGC 6636 from the KPNO 2.1m telescope. A saturated star produced artefacts at lower left, and the colour changes associated with the dust lane in front of the bulge give negative residuals near the nucleus of the larger galaxy. The reported AGN is in the small companion galaxy to the northeast (upper left). The field in each panel is 86 × 119 arcsec showing north to the top and east to the left.

Figure 8. Spectroscopic results on the southern companion to PG 0844+349, shown as in Fig. 2. The traces across the bottom compare the continuum (lower, more compact) and (upper and more spatially extended) Hα intensities along the slit.

spiral arm of the QSO host, without an obvious enhancement as the slit crosses its western arc, so this feature more likely consists of star-forming knots rather than AGN photoionization that fits as well with its very knotty structure compared to the more diffuse and filamentary appearance of EELRs, as in Keel et al. (2017b). These data, and our results on the spiral companion, support either a picture of ionization cones directed near the line of sight and out of the plane of the host galaxy, or one of intermittent high-luminosity accretion phases, perhaps combined with a large physical separation between the pair members. While there remains substantial uncertainty in the line-of-sight separation, this galaxy pair may furnish an
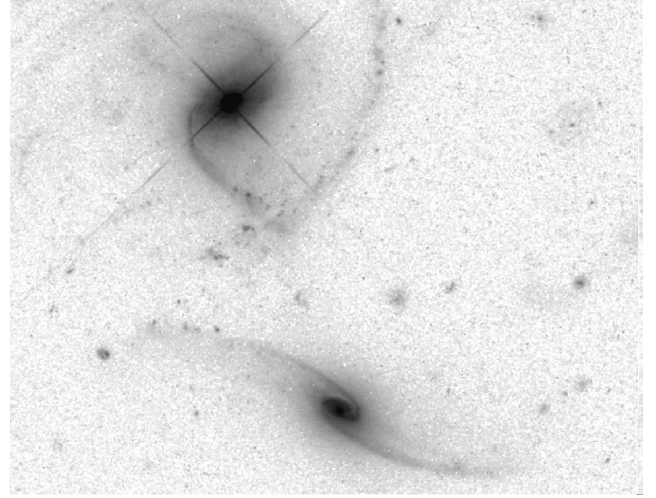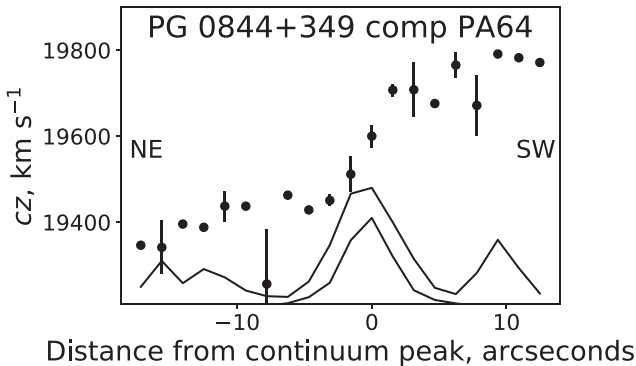

Figure 9. Archival *HST* image of PG 0844+349 and companion galaxy to its south (from program *HST*-GO-9763, PI Barth). This is part of an ACS WFC image in the F625W filter, smoothed with a 3-pixel median for cosmetic reasons. The redshifts are a close match, with the companion at $z = 0.0652$ compared to the luminous AGN at $z = 0.0643$ for a projected velocity difference near 270 km s^{-1}. As expected for trailing spiral arms and the visible dust on the north side, the NE side of the disc is approaching. The area shown spans 38 × 49 arcsec with north at the top.

emission-line version of the same issues encountered in comparing IGM ionization via the direct and transverse proximity effects (as summarized in the Introduction section).

3.1 Low-metallicity 'hidden' AGN-ionized gas

Our primary tool for recognizing AGN-ionized gas is the set of strong emission-line ratios in the 'classical' BPT diagram (Baldwin et al. 1981), based on [O III]/Hβ and [N II]/Hα, incorporating the revised class boundaries from Kewley et al. (2006). These diagnostics become less certain at lower metallicity as [N II] and [S II] become weaker. In this sample, for example, the BPT diagram would classify both SDSS J134203.48+183901.5 and SDSS J135255.67+252859.6 as star-forming galaxies, but broad Hα in the first case, and strong and narrow He II λ4686 in both, mark them as AGN.

4 CONCLUSIONS

Beginning with candidate pairs selected largely from the SDSS archive with the assistance of Galaxy Zoo volunteer participants, we have surveyed a sample of close companion galaxies to AGN for evidence of ionization of their interstellar medium by the external AGN (which we have termed cross-ionization). Such cases can help define the typical cone angles for escape of ionizing radiation, and the typical radiative history of AGN over time-scales ≈10^5 yr. Cho-
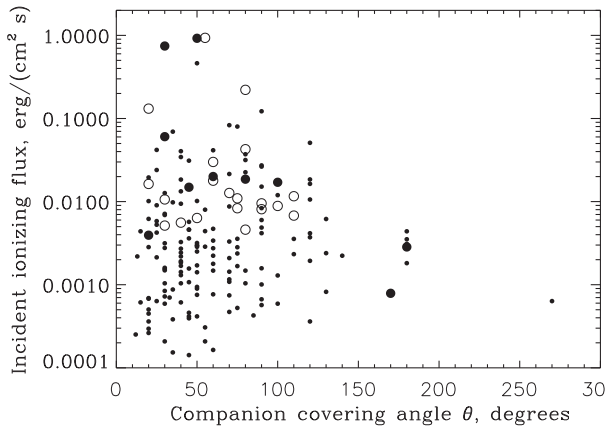
Figure 10. Comparison of subsamples with and without spectroscopic evidence for cross-ionization. The companion covering angle θ is shown as in Fig. 1, while the incident ionizing radiation from the AGN is estimated as in the text, using the median projection correction from Monte Carlo simulations. Small filled circles show all objects in the initial finding list with ionizing flux above 10^{-4} erg cm^{-2} s^{-1} that we did not observe. Large filled circles indicate galaxies with evidence for cross-ionization as in Table 2, while open circles show systems observed spectroscopically and not satisfying our criteria for cross-ionization.

sen on the basis of predicted intensity of incident AGN radiation and fraction of solid angle around the AGN covered by the companion, we observed the 32 most promising systems spectroscopically, of which 10 show spectroscopic evidence for AGN ionization in the companion galaxy or tidal structures and are candidates for cross-ionization. This fraction $(10/32 = 0.31)$ compares reasonably well with our simple geometric estimate ≈ 18 per cent, based on typical ionization cone opening angles $70°$. A larger sample could, for example, place limits on rapid precession of ionization cones, if it were faster than the local recombination time-scales.

Since objects were selected for spectroscopy without prior knowledge of whether we would find evidence of cross-ionization, we can compare the categories with and without such evidence with regard to our selection parameters r and θ to see whether any difference emerges, such as would be expected in the simple case where the local intensity of isotropic AGN radiation controls the amount of excess ionization. Among objects with spectra, the ranges and median values of F_{ion} are similar for the subsets with and without evidence for cross-ionization; for example, the Kolmogorov–Smirnov test suggests rejection of the hypothesis that the F_{ion} distributions are identical only at significance levels well below 90 per cent. This could mean that preferential escape of ionizing radiation or long-term variability are indeed important in determining the ionization environment of AGN. Our data cannot yet distinguish which might have the dominant role, again parallel to studies of the Lyman α proximity effect (Oppenheimer & Schaye 2013, Khrykin et al. 2016; Schmidt et al. 2018).

We illustrate this comparison, extended to both selection parameters, in Fig. 10. The subsamples of our observed galaxies with and without signs of cross-ionization occupy the same regions of the ionizing flux-angle diagram, showing that these two parameters alone do not determine when this effect will be seen. The clustering of observed objects to the top and right reflects our observational priorities.

The systems with the best-attested EELRs in our spectroscopic sample, NGC 5278/9 and NGC 6081, each host dual AGNs of roughly comparable luminosity, and highlight the ambiguities in-

troduced in such pairs. Both AGNs may contribute to the extended ionization; untangling their roles in the likely presence of structured obscuration will require more detailed information on kinematics and the three-dimensional layout of each system.

At this point, our results largely provide a candidate list for detecting cross-ionization. Further work in this direction could be pursued fruitfully with integral-field spectroscopy or narrowband emission-line imaging. Such data could define the regions within which AGN ionization is important. Emission-line imaging at high angular resolution would provide a more sensitive probe for the role of external AGN in companion galaxies, allowing separation of the low-density diffuse ISM (whose ionization balance would be more strongly altered by external radiation) from high-surface-brightness star-forming regions.

Iolkam Du'ag (Kitt Peak), a mountain with particular significance to the Tohono O'odham Nation.

REFERENCES

Stasińska G. et al., 2008, MNRAS, 391, L2978
Abazajian K. N. et al., 2009, ApJS, 182, 543
Adelberger K. L., 2004, ApJ, 612, 706
Afanasiev V. L., Moiseev A. V., 2011, Baltic Astron., 20, 363
Alam S. et al., 2015, ApJS, 219, 12
Allen M. G., Dopita M. A., Tsvetanov Z. I., Sutherland R. S., 1999, ApJ, 511, 686
Antonucci R., 1993, ARAA, 31, 473
Baldwin J. A., Phillips M. M., Terlevich R., 1981, PASP, 93, 5
Barth A. J., Bentz M. C., Greene J. E., Ho L. C., 2008, ApJ, 683, L119
Bianchi S., Fiore F., La Franca F., Mathur S., Matt G., Piconcelli E., Pérez-Torres M. Á. et al., 2013, MNRAS, 435, 2335
Bitsakis T., Dultzin D., Ciesla L., Krongold Y., Charmandaris V., Zezas A., 2015, MNRAS, 450, 3114
Castro C. S., Dors O. L., Cardaci M. V., Hägele G. F., 2017, MNRAS, 467, 1507
Comerford J. M., Greene J. E., 2014, ApJ, 789, 112
Comerford J. M., Barrows R. S., Greene J. E., Müller-Sánchez F., Nevin R., Pooley D., Stern D., Harrison F. et al., 2017, ApJ, 849, 201
Cutri R. M., Wright E. L., Conrow T. et al., 2012, Explanatory Supplement to the WISE All-Sky Data Release Product. http://wise2.ipac.caltech.edu/docs/release/allsky/expsup/sec4_4h.html
Elitzur M., Shlosman I., 2006, ApJ, 648, L101
Elvis M. et al., 1994, ApJS, 95, 1
Filippenko A. V., 1982, PASP, 94, 715
Furlanetto S. R., Lidz A., 2011, ApJ, 735, 117
Gagne J. P. et al., 2014, ApJ, 792, 72
Gonçalves T. S., Steidel C. C., Pettini M., 2008, ApJ, 676, 816
Groves B. A., Heckman T. M., Kauffmann G., 2006, MNRAS, 371, 1559
Heckman T. M., Bothun G. D., Balick B., Smith E. P., 1984, AJ, 89, 958
Heckman T. M., Kauffmann G., Brinchmann J., Charlot S., Tremonti C., White S. D. M., 2004, ApJ, 613, 109
Hutchings J. B., Crampton D., 1990, AJ, 99, 37
Johansson J., Woods T. E., Gilfanov M., Sarzi M., Chen Y.-M., Oh K., 2016, MNRAS, 461, 4505
Kawasaki K., Nagao T., Toba Y., Terao K., Matsuoka K., 2017, ApJ, 842, 44
Keel W. C., 1996, ApJS, 106, 27
Keel W. C., Kennicutt R. C., Jr, Hummel E., van der Hulst J. M., 1985, AJ, 90, 708
Keel W. C., Kennicutt R. C., Jr, van der Hulst J. M., Hummel E., 1989, Eur. South. Obs. Conf. Workshop Proc., 32, 85
Keel W. C., de Grijp M. H. K., Miley G. K., Zheng W., 1994, A&A, 283, 791
Keel W. C., Chojnowski S. D., Bennert V. N. et al., 2012a, MNRAS, 420, 878
Keel W. C., Lintott C. J., Schawinski K. et al., 2012b, AJ, 144, 66
Keel W. C. et al., 2015, AJ, 149, 155
Keel W. C., Oswalt T., Mack P. et al., 2017a, PASP, 129, 015002
Keel W. C., Lintott C. J., Maksym W. P. et al., 2017b, ApJ, 835, 256
Kennicutt R. C., Jr, Roettiger K. A., Keel W. C., van der Hulst J. M., Hummel E., 1987, AJ, 93, 1011
Kewley L. J., Groves B., Kauffmann G., Heckman T., 2006, MNRAS, 372, 961
Khrykin I. S., Hennawi J. F., McQuinn M., Worseck G., 2016, ApJ, 824, 133
Kirkman D., Tytler D., 2008, MNRAS, 391, 1457
Kornilov V. et al., 2014, PASP, 126, 482
Koss M. et al., 2014, MNRAS, 445, 515
Lintott C. J. et al., 2008, MNRAS, 389, 1179
Lintott C. J. et al., 2009, MNRAS, 399, 129

Lipovetsky V. A., Neizvestny S. I., Neizvestnaya O. M., 1988, SoSAO, 55, 5
Liu X., Shen Y., Strauss M. A., Hao L., 2011, ApJ, 737, 101
Martínez M. A., Del Olmo A., Coziol R., Perea J., 2010, AJ, 139, 1199
Miller J. S., Stone R. P. S., 1992, Lick Obs. Technical Report 66. Lick Observatory, Santa Cruz, CA
Moran E. C., Halpern J. P., Bothun G. D., Becker R. H., 1992, AJ, 104, 990
Oppenheimer B. D., Schaye J., 2013, MNRAS, 434, 1063
Petrov G. T., Kovachev B. Z., Mineva V. A., 1985, Ap&SS, 116, 333
Sabater J., Best P. N., Argudo-Fernández M., 2013, MNRAS, 430, 638
Sartori L. F. et al., 2016, MNRAS, 457, 3629
Schawinski K. et al., 2010, ApJ, 724, L30
Schawinski K., Koss M., Berney S., Sartori L. F., 2015, MNRAS, 451, 2517
Schirber M., Miralda-Escudé J., McDonald P., 2004, ApJ, 610, 105
Schirmer M., Diaz R., Holhjem K., Levenson N. A., Winge C., 2013, ApJ, 763, 60
Schmidt T. M., Hennawi J. F., Worseck G., Davies F. B., Lukić Z., Oñorbe J., 2018, ApJ, 861, 122
Schmitt H. R., Donley J. L., Antonucci R. R. J., Hutchings J. B., Kinney A. L., Pringle J. E., 2003, ApJ, 597, 768
Schweizer F., Seitzer P., Kelson D. D., Villanueva E. V., Walth G. L., 2013, ApJ, 773, 148
Secrest N. J., Schmitt H. R., Blecha L., Rothberg B., Fischer J., 2017, ApJ, 836, 183
Stockton A., Fu H., Canalizo G., 2006, NewAR, 50, 694
Storchi-Bergmann T., Schmitt H. R., Calzetti D., Kinney A. L., 1998, AJ, 115, 909
Storchi-Bergmann T., Dall'Agnol de Oliveira B., Longo Micchi L. F. et al., 2018, ApJ, 868, 14
Sun A.-L., et al., 2018, MNRAS, 480, 2302
Tody D., 1986, Proc. SPIEConf. Ser. Vol. 627, SPIE, Bellingham, 733
Veilleux S., Shopbell P. L., Miller S. T., 2001, AJ, 121, 198
Visbal E., Croft R. A. C., 2008, ApJ, 674, 660
Watkins A. E., Mihos J. C., Bershady M., Harding P., 2018, ApJ, 858, L16
Wehrle A. E., Morris M., 1988, AJ, 95, 1689
Wilson A. S., 1996, Vistas Astron., 40, 63
Wright E. L. et al., 2010, AJ, 140, 1868

APPENDIX A: FINDING LIST: LOW REDSHIFT AGN/COMPANION GALAXY PAIRS

For completeness, Table A1 gives relevant properties of all 212 AGN/galaxy pairs considered. Selection properties were projected angle subtended by the companion galaxy around the AGN (θ) and predicted ionizing flux from the AGN at the projected distance of the companion galaxy (F_{ion}). F_{ion} was estimated as was done in Section 2.1, using the [O III] $\lambda 5007$ fluxes calculated, where possible, from the SDSS spectra (based on tabulated line equivalent width EW in Å and local continuum flux F_{cont}, as tabulated in SDSS DR7). Objects are identified both by coordinate designation, with initial J indicating designations used in the Sloan surveys (Alam et al. 2015); and, for SDSS objects, by the Data Release 12 (Alam et al. 2015) numerical ObjID for ease of data retrieval. For compactness, F_{cont} is listed in units 10^{-17} er g cm^{-2} s^{-1} Å^{-1}. F_{ion} is given in arbitrary units, since the quantity has systematic uncertainties as well as projection effects and was used only to rank objects for spectroscopic observation.

In a few cases we used additional sources for emission-line data: Petrov, Kovachev & Mineva (1985) for NGC 6786, Heckman et al. (1984) for the companion of PG 1048+342, and Keel et al. (1985) for NGC 5278/9.

'Type' indicates the AGN type 1 for broad-line objects (as in Sy 1), 2 for narrow-line objects, and 0 for BL Lac objects.

Table A1. Finding list.

Coord ID	SDSS ObjID	Type	z(AGN)	z(compn)	r	θ°	F_{cont}	[O III] EW	F_{ion}	Notes
J001707.95+011506.2	1237678617419710603	2	0.1057	0.1074	11	40	19.90	32.10	22	
J002228.37 − 005830.6	1237657189833900309	1.5	0.1060	0.1060	12	70	9.00	25.80	6.8	
J002944.89+001011.1	1237663784200634427	2	0.0598	0.0594	5	30	28.7	114.3	552	
J005754.03+012013.8	1237678617424166953	2	0.0567		9	30	325	402	6800	UM 293
J011309.59+021716.5	1237680100234887247	1.9	0.0462		72	28				UGC 768
J011448.67 − 002946.0	1237666338653012001	1	0.0338	0.0349	17	45	52.00	12.90	9.8	UGC 793
J011659.06+001933.3	1237666339727015947	1	0.0782	0.0077	9	55	19.20	2.80	2.8	
J013037.75+131252.0	1237649918432116906	2	0.0722	0.0726	16	100	14.00	23.30	5.4	
J020436.76 − 115943.4	1237676674463826080	1.5	0.0726		24	45				
J021209.23+072127.5	1237670016730333231	2	0.1424		6	45	4.20	5.00	2.5	
J022226.11 − 085701.3	1237652900226596935	1	0.1666		3	70	15.20	106.60	759	
J022909.70+010043.0	1237678617434128461	2	0.1283	0.1288	8	30	8.60	11.60	6.6	
J024222.87 − 011009.0	1237660024521556048	2	0.0372	0.0376	23	20	17.20	17.80	2.4	
J025445.35+010308.4	1237678437018108063	2	0.1367	0.1366	9	20	8.70	7.40	3.3	
J025740.83 − 163046.0	1237667244870008884	1	0.0679		5	80				
J030858.44 − 001549.0	1237660240312467582	2	0.2064	0.2069	3	80	5.50	80.00	206	
J033213.20+001546.7	1237666301093675376	1	0.0861	0.0875	8	100	26.40	6.80	11.8	
J072612.51+412233.7	1237673706650796616	1	0.1324		4	70	11.50	6.30	19.1	
J073402.62+433236.9	1237663916261703871	1	0.0831	0.0823	8	45	23.00	15.00	23	
J073906.17+442409.9	1237663915725357374	2	0.1345	0.1408	4	80	12.50	4.10	13.5	
J074408.20+435935.6	1237663530254663877	2	0.1331	0.1348	5	70	7.00	9.00	10.6	
J074429.85+284721.9	1237657119477989769	2	0.1015	0.1025	4	110	12.00	10.30	33	
J074547.87+265537.9	1237657630578376999	1.8	0.1148		8	40	29.00	88.10	168	
J075433.27+204635.2	1237661087490441736	1.8	0.1146	0.1146	8	50	8.00	40.00	21	
J075648.78+501016.6	1237663915728175471	1	0.2366	0.2364	6	45	9.00	13.60	14.3	
J075729.04+351105.9	1237654626788704563	2	0.1117		3	110	16.1	14.1	106	
J080059.77+343412.0	1237674290219450784	2	0.0823	0.0811	8	40	20.00	22.60	30	
J080435.27+363711.5	1237654652024390067	2	0.0913		11	40	15.00	22.80	11.9	
J080514.10+364942.9	1237654652024521006	2	0.0841		16	20	14.00	11.60	2.7	
J080647.76+282512.8	1237658192145744217	2	0.1426		8	75	10.70	6.80	4.8	
J081411.26+144735.4	1237667253453521141	2	0.1572		9	30	9.50	10.88	5.4	
J082017.99+465125.3	1237651250946244661	2	0.0524		8	50	12.00	29.00	23	
J082034.78+153111.2	1237667253454241925	1	0.1438		8	90	14.30	6.50	6.1	
J082913.59+264009.9	1237661087494766877	2	0.0574	0.0571	18	20	26.00	50.00	16.9	
J083049.39+102712.5	1237671262269997354	2	0.0727	0.0720	17	33	18.20	24.20	6.4	
J083116.14+351707.4	1237657629510271237	1.9	0.1601		3	90	10.00	53.20	249	
J083202.71+093759.1	1237671261196255490	2	0.0750		4	130	21.00	10.20	56	
J083224.28+355135.9	1237657775539945655	2	0.1368		6	60	15.00	14.30	25	
J083728.08+391723.7	1237657401878708344	2	0.1147		20	30	17.50	41.80	7.7	
J083848.14+040734.0	1237658423540580569	2	0.0476	0.0484	9	20	72.00	39.70	149	
J083902.96+470756.3	1237654381974716589	2	0.0524	0.0534	18	20	38	71	36	
J084135.08+010156.2	1237650797286850905	2	0.1106		4	80	19.2	400.1	2020	
J084742.44+344504.4	1237658191076720756	1	0.0640	0.0653	22	30	850	3.1	97	PG 0844+349
J084810.11+351534.3	1237664871356891234	2	0.0573	0.0570	4	80	19.5	33.2	170	
J085152.62+522833.0	1237651190821617882	1	0.0645		11	70	14.00	20.40	9.9	
J085820.50+642048.4	1237663917882802416	1	0.1158		5	30	11.50	59.70	116	
J090128.46+352030.1	1237664871894941906	2	0.1053		7	40	30.10	46.90	121	
J090134.48+180943.0	1237667429554585733	2	0.0665	0.0665	9	40	32.00	14.90	25	
J090317.39+100100.5	1237661069779009763	2	0.0619		12	130	31.12	24.10	22	UGC 4748
J090436.92+553602.9	1237651252024836118	1	0.0372		12	75	80.0	32.3	76	
J090604.60+170120.0	1237667485918429442	2	0.1007		8	45	15.00	52.80	52	
J090743.49+013327.9	1237660670347706621	1	0.1643		5	75	18.70	6.90	22	
J090810.33+500923.1	1237654653642801161	1	0.0981	0.1073	13	50	44.00	23.80	26	
J091029.08+203401.9	1237667210510336112	2	0.0289	0.0280	25	270	75.00	11.40	5.8	
J091141.65+370204.1	1237660635988492309	1	0.0865	0.0862	14	30	30.00	39.20	25	
J091319.00+532958.4	1237654383052062933	1.9	0.2549		3	20	13.00	9.30	57	
J091449.05+085321.1	1237660670347706621	1	0.1399		3	75	10.10	6.90	33	
J091540.88+155639.7	1237667735026532578	2	0.1434		9	40	11.00	35.00	20	
J091930.42+133258.7	1237671125373485313	1	0.2291	0.2297	8	120	55.00	9.40	34	
J093044.15+084929.7	1237661064413249768	2	0.1304	0.1300	4	40	11.00	108.40	314	
J093811.95+045356.5	1237658298454180052	1.8	0.1626		4	180	12.00	10.20	32	
094542.04 − 141934.8		2	0.0077	0.0081	87	20				NGC 2992
J094716.12+534944.8	1237655108368597025	2	0.0383		15	90	16.20	47.60	14.4	

Coord ID	SDSS ObjID	Type	z(AGN)	z(compn)	r	θ°	F_{cont}	[O III] EW	F_{ion}	Notes
J094741.58+633939.2	1237651540315930774	2	0.1390		3	50	16.00	12.40	93	
J095847.90+144526.2	1237671261742694538	2	0.0767		7	60	15.50	10.10	13.5	
J095958.22+030232.7	1237654599952760951	2	0.0907	0.0906	17	40	20.00	44.70	13.0	
J100531.67+183939.0	1237667782284017791	2	0.0779	0.0780	7	70	14.00	10.90	13.1	
J100534.70+392852.8	1237660772882907153	1	0.1408		12	25	22.00	9.00	5.8	
J100602.50+071131.8	1237658300604743843	2	0.1205	0.1218	5	80	25.00	80.50	339	
J101043.36+061201.4	1237658423550607494	1	0.0978		4	20	39.3	116.1	1200	
J101202.59+301303.0	1237665097393963129	1	0.0498		12	70	55.00	49.60	80	
J101439.55 − 004951.2	1237654669200326683	2	0.0491	0.0483	19	20	41.00	13.20	6.3	UGC 5528
J101653.82+002857.0	1237654670811201558	2	0.1163		2	50	20.90	191.70	4220	
J101932.86 − 032014.9	1237650803195248686	1	0.0500	0.0492	37	35				Mkn 1253
J102027.52+135530.1	1237661070861140238	2	0.1449		6	15	16.00	21.40	40	
J102250.45+495936.5	1237657858213871668	2	0.1155		16	55	11.70	9.70	1.9	
J102536.43+371317.1	1237664669509550195	2	0.0608		5	180	34.00	7.00	40	
J102850.92+163917.9	1237671262819713088	2	0.1720		5	75	5.40	16.80	15.3	
J102940.71+015555.1	1237651753463578759	2	0.0412	0.0418	40	50	37.50	38.00	3.8	UGC 5694
J103000.93+085202.6	1237660583909720086	2	0.0522		20	35	63.00	12.00	8.0	
J103011.81+035410.7	1237654604787745026	2	0.0510		11	50	22.00	11.20	8.6	
J103216.14+505120.0	1237657589242396682	1	0.1737		3	120	22.40	16.10	169	
J103600.37+013653.5	1237651752927363244	2	0.1068		7	25	42.00	105.90	382	
J103607.13+191048.1	1237667781213421682	2	0.1117		10	70	14.00	7.30	4.3	
J103655.60+380321.4	1237662226206228529	2	0.0507	0.0500	29	40	48.60	23.20	5.6	
J103734.22+140120.5	1237661070326104198	2	0.2060		5	20	23.00	46.00	178	
J103819.51+161445.1	1237671261746888940	2	0.1359		3	35	13.00	14.70	89	
J103825.16 − 002331.1	1237654669739819119	2	0.0963		4	180	14.00	4.50	16.6	
J104232.05+050241.9	1237654602104897626	2	0.0272	0.0273	9	180	26.0	19.4	26	NGC 3341
J104519.45+123839.3	1237661068179406916	2	0.0394	0.0398	8	60	45.00	14.50	43	
J105030.47+232931.4	1237667538012602552	1.8	0.0604		5	50	18	19.2	58	
J105128.41+335850.8	1237665129609691296	1	0.1828		5	55	9.00	17.30	26	
J105143.89+335926.7	1237665129609756690	1	0.1671	0.1670	4	40	81.00	17.30	369	PG 1048+342
J105203.60+060349.4	1237658422481387583	1.8	0.1281	0.1285	11	15	18.00	9.00	5.6	
J105222.48+180711.1	1237668288550076449	1	0.1322		2	120	26.00	17.00	466	
J105418.31+181344.7	1237668288550273059	2	0.0811		10	30	16.00	20.90	14.1	
J105434.78+302211.7	1237665329844322346	2	0.1055		13	20	16.00	15.50	6.2	
J105503.48+425136.8	1237661850925793371	2	0.0592	0.0590	11	50	35.00	22.40	27	
J105505.07+414944.8	1237661871322955907	2	0.1077		2	120	8.20	17.30	149	
J105521.02+291849.3	1237667212668895318	2	0.1408		3	30	6.50	40.00	122	
J105738.07+082007.5	1237671930135445716	2	0.0371	0.0366	26	60	15.00	7.90	0.7	
J110017.99+100256.8	1237671932283322446	2	0.0360	0.0361	20	170	40.00	17.10	7.2	UGC 6081
J110157.90+101739.3	1237658493883711561	1.5	0.0341	0.0347	31	80	48.3	198.5	42	Tol 1059+105
J110301.26+120543.0	1237665195024632306	2	0.1184		6	45	16.00	22.40	42	
J110427.30+381232.2	1237662224597909569	0	0.0302	0.0313	12	20				Mkn 421
J110525.11+215229.6	1237667783364051073	2	0.1475		4	80	11.80	93.00	289	
J110544.44+195746.3	1237668294982500461	2	0.1043		4	90	16.00	13.00	55	
J110550.53+205113.3	1237667734501326907	2	0.1015		8	25	22.00	26.70	39	
J110612.16+061347.6	1237658422482895003	2	0.0979	0.0986	17	20	12.00	23.20	4.1	
J110639.11+433620.9	1237661872934682808	2	0.1185	0.1186	5	110	23.40	5.40	21	
J110816.45+293210.5	1237667255082745989	2	0.0466	0.0467	9	60	25.00	12.50	16	
J111118.04+352308.3	1237664817671438525	2	0.0250		9	45	45.00	14.10	33	
J111159.48+013643.4	1237651752931360818	1.9	0.1108	0.1099	7	30	13.00	25.80	29	
J111545.61+065143.2	1237661971178586191	1	0.1492		9	25	12.00	85.30	53	
J111623.16+532413.3	1237657889782413395	2	0.1123	0.1125	2	100	17.00	6.10	109	
J111943.34+451612.6	1237661852538568731	2	0.2036	0.2030	6	60	10.00	323.60	379	
J112336.17+521810.0	1237658857681260680	2	0.1579		11	30	12.00	32.50	13.6	
J112353.48+655133.5	1237651537636032650	2	0.1326		7	50	8.80	10.90	8.2	
J112525.71+533344.4	1237658800960700483	2	0.0804	0.0808	17	50	26.00	18.30	6.9	
J112602.45+343448.1	1237665025437139019	1.5	0.1113	0.1115	11	140	21.00	27.90	20	
J112949.25+172020.2	1237668585971253453	1	0.1571		4	45	12.00	41.60	132	
J113003.10+655629.3	1237651271361495049	1	0.1326		4	90	19.60	26.80	138	
J113215.11+244516.8	1237667550885314686	1	0.1711		4	50	7.40	6.60	12.9	
J113240.25+525701.3	1237657630599872600	2	0.0266	0.0271	34	30	180	71.4	47	Mkn 176
J113321.04+373944.3	1237664819821019315	2	0.1754		6	30	7.90	10.30	9.5	
J113323.97+550415.8	1237658802571968533	1	0.0085	0.0078	8	>120	1.30	11.90	1.0	Mkn 177

Coord ID	SDSS ObjID	Type	z(AGN)	z(compn)	r	$\theta°$	$F_{\rm cont}$	[O III] EW	$F_{\rm ion}$	Notes
J113342.78+353135.4	1237665026511601678	1	0.2018	0.2036	4	90	31.00	29.50	241	
J113443.24+153848.0	1237661070869069974	2	0.0698	0.0693	12	50	30.00	30.80	27	
J113800.25+482623.2	1237658611445530792	1	0.1000	0.1002	4	120	15.00	24.50	97	
J113858.89+141253.2	1237664289924055180	2	0.0805		8	75	22.6	67.3	100	
J113942.52+315433.7	1237665368509710424	1.5	0.0089	0.0090	84	30	50.00	1.00		NGC 3786
J114154.76+465656.9	1237660635464466499	2	0.0728		4	90	1.60	12.40	5.2	
J114252.83+325124.2	1237665369583779929	2	0.0666	0.0661	15	40	27	101.8	51	
J114719.94+075243.1	1237661972255736072	2	0.0826	0.0821	15	30	27.00	28.90	14.6	
J115112.99+064105.9	1237661970645581860	1	0.0768	0.0807	13	80	25.00	15.30	9.5	
J115535.35+125253.9	1237661813346009111	1	0.1216		8	25	57.00	5.20	19.5	
J120041.39+314746.2	1237665226229940236	2	0.1159		4	55	80	400	8530	
J120149.74 − 015327.5	1237650762390765695	1	0.0907		5	50	18.0	147.2	8426	
J120235.97+372157.8	1237664818749767887	2	0.1975		6	75	12.00	18.40	26	
J120336.87+200629.2	1237668298202415270	2	0.2121		3	90	11.40	209.00	1115	
J120349.20+020556.9	1237651753473867953	1.5	0.0812		8	40	23.50	10.90	17	
J120655.62+501737.4	1237658205047488538	1.5	0.0621	0.0633	50	35	35.50	22.90	1.4	
J120712.57+165809.6	1237668623548022885	2	0.0723	0.0737	13	85	24.00	6.51	3.9	
J120836.75+223934.3	1237667782833602610	1	0.1997		3	90	18.30	8.90	76	
J121015.67+262837.4	1237667441896390838	2	0.1041		8	20	38.00	37.00	93	
J121151.12+443327.6	1237661850395017428	2	0.1003		15	120	16.00	11.00	3.3	
J121155.63+372113.4	1237664818750619663	2	0.0838	0.0834	8	90	14.00	41.30	38	
J121303.35+513855.2	1237657855537053802	2	00849		7	100	22.0	42.6	81	
J121418.25+293146.7	1237667253478424610	2	00632	0.0640	7	100	31.	58.5	156	Was 49
J121522.77+414620.9	1237661966355988618	1	0.1963		5	45	17.00	99.10	284	
J121749.78+354449.6	1237665025978663019	2	0.0881	0.0880	4	120	14.00	10.30	38	
J121943.13+132659.9	1237661813885436022	2	0.0647	0.0645	11	110	25	71	62	
J121953.10+554506.8	1237658918529925220	1	0.1075		11	25	19.50	70.90	48	
J122026.09+044631.9	1237655125009498294	2	0.0811	0.0803	45	12	8.00	200.00	3.3	
J122157.16+080515.1	1237661972259537090	2	0.0718		12	45	30.20	47.60	42	
J122500.80+014401.8	1237651752939290772	2	0.0897	0.0898	25	45	28.00	20	3.8	
J122744.56 − 015140.2	1237650371558703219	1	0.1484		5	40	22.60	22.60	86	
J123152.05+450443.1	1237661872941367322	1	0.0622	0.0621	20	60	55.00	12.00	7.0	
J123351.61+195311.6	1237667915421778099	2	0.0737	0.0735	7	50	15.00	12.10	16	
J123507.49+171509	1237668589724631143	2	0.0894	0.0898	11	40	19.30	26.00	17	
J124214.47+141147.0	1237662524694462694	2	0.1574		15	20	14.00	17.60	4.6	
J124322.55+373858.0	1237664819290177687	2	0.0859	0.0865	6	90	37	17.3	74	
J124406.59+652925.5	1237654610679955615	2	0.1071		4	75	21.50	129.00	730	
J130116.09 − 032829.0	1237650369414889508	2	0.0864	0.0867	11	70	34.80	24.90	30	
J130240.41+514644.4	1237661958293028932	2	0.0539	0.0550	110	12	28.20	57.70	0.6	UGC 8151
J130354.71 − 030631.8	1237650760786903297	2	0.0778		6	60	36.2	38.6	163	
J130600.68+000125.0	1237648704582844527	2	0.1379	0.1377	13	20	11.00	94.60	26	
J131135.65+142447.1	1237662525234479221	1	0.1140		9	45	60.00	42.10	131	
J131318.92+504001.7	1237661957220139201	2	0.1585		6	55	13.20	26.10	40	
J131517.26+442425.5	1237661851473739819	2	0.0355	0.0355	37	90	110.00	27.20	9.2	
J131639.74+445235.0	1237661852010676264	2	0.0906	0.0915	12	25	45.00	166.50	219	
J131854.19+221825.5	1237667783377551471	2	0.1818		3	90	8.20	11.60	45	
J132751.63+330638.1	1237665127476428926	2	0.1412		2	70	13.70	13.60	196	
J133920.85+393224.3	1237662305112293614	2	0.2240		3	90	39.00	200.00	3650	
J134143.75+554025.5	1237661387065786478	2	0.0251	0.0253	38	45	3100.00	15.00	136	NGC 5278/9
J134203.48+183901.5	1237668271899738298	1.8	0.0845		5	80	17.6	134.4	399	
J134234.31+191338.9	1237668272436674636	1	0.0866	0.0866	9	180	49.00	11.10	28	
J134730.70+603743.1	1237655369829580934	1	0.1433	0.1438	5	30	15.20	25.40	65	
J134736.39+173404.6	1237668316456288331	2	0.0447	00451	10	90	40	51.9	87	
J134955.48+084039.6	1237662236939256056	2	0.0670		10	30	220.00	6.80	63	
J135255.67+252859.6	1237665531709554737	1	0.0636		5	60	40.00	40.70	274	
J135429.05+132757.2	1237662529526890706	2	0.0633		9	60	8.4	420	183	
J135713.88+115951.0	1237662199886184522	2	0.0205	0.0205	85	30	97.30	4.60	0.3	
J140944.19+100429.7	1237662239088836793	2	0.0958	0.0951	26	12	12.40	30.40	2.3	
J141041.49+223337.0	1237667911678099640	1	0.1725		3	35	31.50	43.00	634	
J141104.81 − 001906.6	1237648704053051635	2	0.1387	0.1390	5	60	11.50	16.00	31	
J141447.15 − 000013.1	1237648721245503521	2	0.0475	0.0474	5	70	24.0	28.8	116	
J141946.07+650353.2	1237674479196242084	1	0.1479		4	70	25.00	50.00	329	

Table A1 – *continued*

Coord ID	SDSS ObjID	Type	z(AGN)	z(compn)	r	$\theta°$	F_{cont}	[O III] EW	F_{ion}	Notes
J142255.49 − 001711.4	1237648704054362331	2	0.1302		5	40	5.00	200.00	168	
J142755.36 − 003341.8	1237648720710074546	2	0.0795	0.0792	7	50	15.00	22	29	
J142802.22+062619.5	1237655744015368412	2	0.1155		13	45	8.90	18.80	4.2	
J143454.21+334934.5	1237662661597659257	2	0.0578	0.0587	14	35	30.00	5.4	3.5	
J143515.65+023221.6	1237651754564190252	1	0.3048		6	25	46.70	15.10	82	
J144213.96+231844.6	1237665532251406538	1	0.1830		9	30	6.10	5.90	1.9	
J144248.27+120040.3	1237662529532133399	0	0.1631		2	120	42.00	0.40	18	
J144733.17 − 013844.3	1237655499209310386	2	0.0428	0.0427	73	26	28.70	3.90	0.1	
J144937.71+184159.5	1237667783386988590	2	0.0321	0.0320	29	45	89.40	3.00	1.3	
J145002.97+255441.2	1237665178450788549	1.8	0.0604		7	60	15.00	15.80	20.4	
J145051.51+050652.1	1237651822714028249	2	0.0275	0.0282	21	55	100.00	76.40	73	NGC 5765
174659.8 +683637		1	0.0630	0.0623	7	120				Kaz 163
182205.11+663719.2		2	0.0155	0.0146	24	150				Kaz 199 NGC 6636
191152.98+731929.5		2	0.0250	0.0252	85	10		13.30		NGC 6786
J220041.34+103308.0	1237678859532566564	2	0.0266		3	120				Mkn 520
J220555.01 − 000755.2	1237663543146643720	2	0.0945	0.0939	13	60	13.30	4.40	1.5	
J220701.98+101400.8	1237678876177072140	2	0.0266	0.0266	13	75				NGC 7212
J225057.27 − 085410.8	1237652600111366327	1.8	0.0650	0.0644	6	30	35.00	23.50	96.3	
J225452.22+004631.3	1237663445442691192	1	0.0909	0.0912	11	40	57.50	7.70	15.4	
J225823.29+001603.8	1237663444906213507	2	0.1542	0.1543	10	45	16.10	5.30	3.6	
J230315.61+085226.0	1237679034548551752	1	0.0163	0.0160	71	50	0.00		0.0	NGC 7469
J230443.47 − 084108.6	1237653438155128872	1	0.0470	0.0473	63	13	172.00	109.80	20	Mkn 926
J232756.70+084644.3	1237679034014367754	2	0.0289	0.0295	45	80				NGC 7674
J234428.33+010829.7	1237656909037699193	2	0.1206	0.1167	11	40	13.90	19.60	9.5	

This paper has been typeset from a TEX/LATEX file prepared by the author.